

Chapter 8

Fourth-Order Statistics: Weak Fluctuation Theory

8.1	Introduction	259
8.2	Scintillation Index	261
	8.2.1 Inner scale models	265
	8.2.2 Numerical results	267
8.3	Beam Wander and Scintillation	269
	8.3.1 Untracked beam	274
	8.3.2 Tracked beam	275
8.4	Covariance Function of Irradiance	279
8.5	Temporal Spectrum of Irradiance	282
	8.5.1 Plane wave	282
	8.5.2 Spherical wave	283
	8.5.3 Gaussian-beam wave	284
8.6	Phase Fluctuations	288
	8.6.1 Phase variance	289
	8.6.2 Phase structure function	291
	8.6.3 Covariance function	294
	8.6.4 Temporal power spectrum	296
8.7	Slant Paths	299
	8.7.1 Irradiance fluctuations	299
	8.7.2 Phase fluctuations	301
8.8	Summary and Discussion	302
8.9	Worked Examples	308
	Problems	313
	References	318

Overview: In this chapter we examine various fourth-order statistical quantities like the *scintillation index* and the *irradiance covariance function*. Knowledge of the scintillation index is crucial for determining system performance in a laser communication system or laser radar link (Chaps. 11 and 13). In particular, *beam wander* may be an important factor for scintillation, depending on whether or not the beam is tracked (i.e., whether beam wander is removed), and whether it is collimated or focused.

All expressions developed in this chapter are restricted to *weak irradiance fluctuation regimes* for which the *Rytov method* can be used. For this case the scintillation index is directly related to the *log-amplitude variance* studied in most early publications. In Chap. 9 we will expand these results into the *moderate-to-strong fluctuation regimes* by employing the extended Rytov method (Chap. 5). Many results developed here are based on the *Kolmogorov power-law spectrum* for reasons of mathematical tractability. However, in attempting to compare scintillation models with measured data taken in outdoor experiments, for example, it may be necessary to use the more general models found in Appendix III based on the *modified atmospheric spectrum*. This spectrum model features both inner scale and outer scale parameters, and the high wave number “bump.” This so-called “bump” near the start of the dissipation regime in the spatial power spectrum can have a profound effect on irradiance fluctuations (leading to potentially large scintillation values).

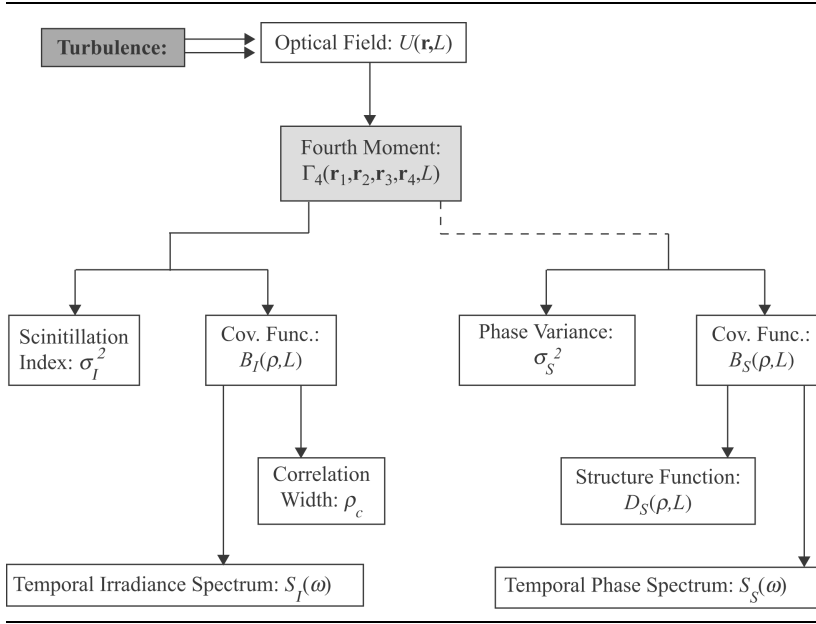
The *correlation width* ρ_c , determined from the irradiance covariance function, identifies the maximum receiver aperture size that will act like a “point receiver.” Aperture sizes larger than ρ_c will experience some form of “aperture averaging,” which in effect reduces the scintillation experienced by the receiver photodetector (see Chaps. 10 and 11).

By invoking the *frozen-turbulence hypothesis*, we can infer the *temporal covariance function* from which we calculate the *temporal spectrum* of irradiance fluctuations. In weak fluctuations, we find the spectral width is determined by the transverse wind velocity scaled by the first Fresnel zone.

Last, we examine *phase fluctuations* and the *phase covariance function* in a manner that parallels our treatment of irradiance fluctuations. Knowledge of atmospheric phase fluctuations is important in the use of coherent heterodyne receivers and for phase modulation techniques applied to optical communications. We also briefly discuss the phase temporal spectrum.

Flowchart

In Chaps. 8 and 9 we examine specializations of the fourth moment of the optical field from which we can deduce statistics concerning irradiance fluctuations and phase fluctuations. The flowchart provided in Table 8.1 below is intended to

Table 8.1 Flowchart for Chaps. 8 and 9.

help the reader identify how these various statistical quantities are related back to the optical field in the presence of optical turbulence. Unlike amplitude (or irradiance) fluctuations, the phase is not a direct specialization of the fourth-order field moment $\Gamma_4(\mathbf{r}_1, \mathbf{r}_2, \mathbf{r}_3, \mathbf{r}_4, L)$. For this reason we have shown the connection between the phase statistics and the fourth-order moment with a dashed line rather than a solid line.

8.1 Introduction

In the context of Rytov theory, many early investigations into the statistical characteristics of an optical wave propagating through atmospheric turbulence were concerned with the *log-amplitude variance* σ_χ^2 or *log-irradiance variance* $\sigma_{\ln I}^2 = 4\sigma_\chi^2$. Under weak fluctuation conditions, the *normalized variance of irradiance* (i.e., *scintillation index*) σ_I^2 is approximately equal to the log-irradiance variance, i.e., $\sigma_I^2 \cong \sigma_{\ln I}^2$. The majority of these early studies also centered on plane wave and spherical wave models, both of which are limiting cases of the more general Gaussian-beam wave model. The governing integrals for beam-wave propagation were first formulated by Schmeltzer [1] using the Rytov method. Fried and Seidman [2] solved these integrals for the log-amplitude variance at the beam centerline (optical axis) using a Kolmogorov power-law spectrum model for refractive-index fluctuations. Their analysis discussed the transition of a collimated beam from spherical wave propagation to plane wave

propagation for increasing aperture size. They also predicted a substantial reduction in scintillation for a large-aperture focused beam. Ishimaru [3] used spectral analysis techniques to obtain expressions for several statistical quantities, including the log-amplitude variance. His general results are valid for points off the beam centerline and, for a focused beam, predict the same scintillation reduction on the beam centerline as that of Fried and Seidman. It is now known that this predicted behavior in scintillation for a large-aperture focused beam has limitations. That is, whereas Rytov theory predicts decreasing scintillation levels along the optical axis, it simultaneously predicts a substantial increase in scintillation over a short radial distance from the optical axis that is physically unrealistic (Section 8.2.1).

In the last two chapters we considered first- and second-order field moments and various specializations of the latter. Here and in Chap. 9 we build on that analysis by considering specializations of the fourth-order field moment that lead to the scintillation index, covariance function of irradiance, and the temporal spectrum of irradiance fluctuations. The general *fourth-order cross-coherence function* for a beam wave that has propagated a distance L is defined by the ensemble average

$$\Gamma_4(\mathbf{r}_1, \mathbf{r}_2, \mathbf{r}_3, \mathbf{r}_4, L) = \langle U(\mathbf{r}_1, L)U^*(\mathbf{r}_2, L)U(\mathbf{r}_3, L)U^*(\mathbf{r}_4, L) \rangle, \quad (1)$$

which can be expressed in the form

$$\begin{aligned} \Gamma_4(\mathbf{r}_1, \mathbf{r}_2, \mathbf{r}_3, \mathbf{r}_4, L) &= U_0(\mathbf{r}_1, L)U_0^*(\mathbf{r}_2, L)U_0(\mathbf{r}_3, L)U_0^*(\mathbf{r}_4, L) \\ &\quad \times \langle \exp[\psi(\mathbf{r}_1, L) + \psi^*(\mathbf{r}_2, L) + \psi(\mathbf{r}_3, L) + \psi^*(\mathbf{r}_4, L)] \rangle \\ &= \Gamma_2(\mathbf{r}_1, \mathbf{r}_2, L)\Gamma_2(\mathbf{r}_3, \mathbf{r}_4, L)\exp[E_2(\mathbf{r}_1, \mathbf{r}_4) + E_2(\mathbf{r}_3, \mathbf{r}_2) \\ &\quad + E_3(\mathbf{r}_1, \mathbf{r}_3) + E_3^*(\mathbf{r}_2, \mathbf{r}_4)]. \end{aligned} \quad (2)$$

Here, Γ_2 is the mutual coherence function (MCF) defined by Eq. (35) in Chap. 6 for the optical field $U(\mathbf{r}, L)$, the asterisk denotes complex conjugate, and the quantities E_2 and E_3 are defined, respectively, by

$$\begin{aligned} E_2(\mathbf{r}_1, \mathbf{r}_2) &= 4\pi^2 k^2 L \int_0^1 \int_0^\infty \kappa \Phi_n(\kappa) J_0[\kappa|(1 - \bar{\Theta}\xi)\mathbf{p} - 2i\Lambda\xi\mathbf{r}|] \\ &\quad \times \exp\left(-\frac{\Lambda L \kappa^2 \xi^2}{k}\right) d\kappa d\xi, \end{aligned} \quad (3)$$

$$\begin{aligned} E_3(\mathbf{r}_1, \mathbf{r}_2) &= -4\pi^2 k^2 L \int_0^1 \int_0^\infty \kappa \Phi_n(\kappa) J_0[(1 - \bar{\Theta}\xi - i\Lambda\xi)\kappa\mathbf{r}] \\ &\quad \times \exp\left(-\frac{\Lambda L \kappa^2 \xi^2}{k}\right) \exp\left[-\frac{iL\kappa^2}{k}\xi(1 - \bar{\Theta}\xi)\right] d\kappa d\xi, \end{aligned} \quad (4)$$

where $\xi = 1 - z/L$. As before, we will specify free space Gaussian beam characteristics by the following sets of beam parameters (recall Section 6.2.1)

$$\Theta_0 = 1 - \frac{L}{F_0}, \quad \Lambda_0 = \frac{2L}{kW_0^2}, \quad (5)$$

$$\Theta = 1 + \frac{L}{F} = \frac{\Theta_0}{\Theta_0^2 + \Lambda_0^2}, \quad \left(\bar{\Theta} = -\frac{L}{F} = 1 - \Theta \right),$$

$$\Lambda = \frac{2L}{kW^2} = \frac{\Lambda_0}{\Theta_0^2 + \Lambda_0^2}. \quad (6)$$

Equations (5), called the *transmitter beam parameters*, describe the beam radius W_0 and radius of curvature of the phase front F_0 at the exit aperture of the transmitter. Similarly, Eqs. (6) describe the beam radius W and phase front radius of curvature F at the receiver plane and are therefore called the *receiver beam parameters*. The limiting case of a plane wave is obtained by specifying $\Theta = 1$ and $\Lambda = 0$, and the spherical wave limit is obtained by specifying $\Theta = \Lambda = 0$.

By setting $\mathbf{r}_1 = \mathbf{r}_2 = \mathbf{r}_3 = \mathbf{r}_4 = \mathbf{r}$, the fourth-order coherence function (2) yields the *second moment of the irradiance*

$$\begin{aligned} \langle I^2(\mathbf{r}, L) \rangle &= \Gamma_4(\mathbf{r}, \mathbf{r}, \mathbf{r}, \mathbf{r}, L) \\ &= \langle I(\mathbf{r}, L) \rangle^2 \exp\{2 \operatorname{Re}[E_2(\mathbf{r}, \mathbf{r}) + E_3(\mathbf{r}, \mathbf{r})]\}, \end{aligned} \quad (7)$$

where Re denotes the real part of the argument. The *covariance function of irradiance* is a two-point statistic defined by the normalized quantity (see Section 8.4)

$$\begin{aligned} B_I(\mathbf{r}_1, \mathbf{r}_2, L) &= \frac{\Gamma_4(\mathbf{r}_1, \mathbf{r}_1, \mathbf{r}_2, \mathbf{r}_2, L) - \Gamma_2(\mathbf{r}_1, \mathbf{r}_1, L)\Gamma_2(\mathbf{r}_2, \mathbf{r}_2, L)}{\Gamma_2(\mathbf{r}_1, \mathbf{r}_1, L)\Gamma_2(\mathbf{r}_2, \mathbf{r}_2, L)} \\ &= \frac{\Gamma_4(\mathbf{r}_1, \mathbf{r}_1, \mathbf{r}_2, \mathbf{r}_2, L)}{\Gamma_2(\mathbf{r}_1, \mathbf{r}_1, L)\Gamma_2(\mathbf{r}_2, \mathbf{r}_2, L)} - 1, \end{aligned} \quad (8)$$

which for $\mathbf{r}_1 = \mathbf{r}_2 = \mathbf{r}$ reduces to the *scintillation index*

$$\sigma_I^2(\mathbf{r}, L) = \frac{\langle I^2(\mathbf{r}, L) \rangle}{\langle I(\mathbf{r}, L) \rangle^2} - 1. \quad (9)$$

Note that (9) is the irradiance variance scaled by the square of the mean irradiance. In this chapter we confine our attention to statistical quantities like the scintillation index under the restriction of *weak irradiance fluctuations*, and extend the analysis in Chap. 9 to include the case of *strong irradiance fluctuations*.

8.2 Scintillation Index

Fluctuations in received irradiance resulting from propagation through atmospheric turbulence is commonly described as “scintillation.” The term scintillation

includes the temporal variation in received irradiance (such as star twinkle) and spatial variation within a receiver aperture (such as speckle).

Because the logarithm of the amplitude of an optical wave was assumed to be governed by Gaussian statistics in the weak fluctuation regime, it was natural in early studies to concentrate on the log-amplitude variance rather than on the irradiance variance itself. The *log amplitude* of the optical wave is related to the atmospherically induced complex phase perturbation according to (Section 5.6.2)

$$\chi(\mathbf{r}, L) = \frac{1}{2}[\psi(\mathbf{r}, L) + \psi^*(\mathbf{r}, L)], \quad (10)$$

where $\psi(\mathbf{r}, L) = \psi_1(\mathbf{r}, L) + \psi_2(\mathbf{r}, L)$ includes both first-order and second-order perturbations. However, only the first-order log-amplitude perturbation χ_1 is necessary to calculate the log-amplitude variance. That is, retaining terms only up to second order in the following statistical moments, the *log-amplitude variance* is defined by

$$\begin{aligned} \sigma_\chi^2(\mathbf{r}, L) &= \langle \chi_1^2(\mathbf{r}, L) \rangle - \langle \chi_1(\mathbf{r}, L) \rangle^2 \\ &= \frac{1}{2} \operatorname{Re}[\langle \psi_1(\mathbf{r}, L) \psi_1^*(\mathbf{r}, L) \rangle + \langle \psi_1(\mathbf{r}, L) \psi_1(\mathbf{r}, L) \rangle] \\ &= \frac{1}{2} \operatorname{Re}[E_2(\mathbf{r}, \mathbf{r}) + E_3(\mathbf{r}, \mathbf{r})]. \end{aligned} \quad (11)$$

Consequently, for *homogeneous* and *isotropic turbulence*, the log-amplitude variance for a Gaussian-beam wave based on (3) and (4) takes the form

$$\begin{aligned} \sigma_\chi^2(\mathbf{r}, L) &= 2\pi^2 k^2 L \int_0^1 \int_0^\infty \kappa \Phi_n(\kappa) \exp\left(-\frac{\Lambda L \kappa^2 \xi^2}{k}\right) \\ &\quad \times \left\{ I_0(2\Lambda r \kappa \xi) - \cos\left[\frac{L \kappa^2}{k} \xi(1 - \bar{\Theta} \xi)\right] \right\} d\kappa d\xi, \end{aligned} \quad (12)$$

where $I_0(x)$ is a modified Bessel function of the first kind (see Appendix I).

When the log-amplitude variance is sufficiently small ($\sigma_\chi^2 \ll 1$), the *scintillation index* (9) is related by (see Probs. 19 and 20 in Chap. 5)

$$\sigma_I^2(\mathbf{r}, L) = \exp\left[4\sigma_\chi^2(\mathbf{r}, L)\right] - 1 \cong 4\sigma_\chi^2(\mathbf{r}, L), \quad (13)$$

and, therefore, we can write

$$\begin{aligned} \sigma_I^2(\mathbf{r}, L) &= 8\pi^2 k^2 L \int_0^1 \int_0^\infty \kappa \Phi_n(\kappa) \exp\left(-\frac{\Lambda L \kappa^2 \xi^2}{k}\right) \\ &\quad \times \left\{ I_0(2\Lambda r \kappa \xi) - \cos\left[\frac{L \kappa^2}{k} \xi(1 - \bar{\Theta} \xi)\right] \right\} d\kappa d\xi. \end{aligned} \quad (14)$$

For interpretation purposes, it is convenient to express the scintillation index (14) as a sum of radial and longitudinal components in the form

$$\begin{aligned}\sigma_I^2(\mathbf{r}, L) &= \sigma_{I,r}^2(\mathbf{r}, L) + \sigma_{I,l}^2(L) \\ &= 4\sigma_r^2(\mathbf{r}, L) + \sigma_{I,l}^2(L),\end{aligned}\quad (15)$$

where we simply rearrange the integrals in (14) to identify

$$\begin{aligned}\sigma_{I,r}^2(\mathbf{r}, L) &= 8\pi^2 k^2 L \int_0^1 \int_0^\infty \kappa \Phi_n(\kappa) \exp\left(-\frac{\Lambda L \kappa^2 \xi^2}{k}\right) \\ &\quad \times [I_0(2\Lambda r \xi \kappa) - 1] d\kappa d\xi,\end{aligned}\quad (16)$$

$$\begin{aligned}\sigma_{I,l}^2(L) &= 8\pi^2 k^2 L \int_0^1 \int_0^\infty \kappa \Phi_n(\kappa) \exp\left(-\frac{\Lambda L \kappa^2 \xi^2}{k}\right) \\ &\quad \times \left\{1 - \cos\left[\frac{L \kappa^2}{k} \xi(1 - \bar{\Theta} \xi)\right]\right\} d\kappa d\xi.\end{aligned}\quad (17)$$

The quantity $\sigma_{I,r}^2(\mathbf{r}, L) = 4\sigma_r^2(\mathbf{r}, L)$, called the *radial component* of the scintillation index, is directly related to the radial term $\sigma_r^2(\mathbf{r}, L)$ that appeared in Eq. (36) in Chap. 6 for the MCF. In the present context, this quantity physically describes the off-axis contribution to the scintillation index. Note that the radial component vanishes at the beam centerline ($r = 0$) or when $\Lambda = 0$, the latter case corresponding to an infinite wave such as a plane wave or spherical wave. The quantity $\sigma_{I,l}^2(L)$ defined by Eq. (17) is called the *longitudinal component* of the scintillation index, which is constant throughout the beam cross section in any transverse plane. To emphasize the fact that the longitudinal component corresponds to the on-axis scintillation index, we sometimes write it as $\sigma_I^2(0, L)$.

For the special case of a Kolmogorov spectrum [Eq. (18) in Chap. 3], the radial term (16) leads to (see Prob. 9 in Chap. 6)

$$\sigma_{I,r}^2(\mathbf{r}, L) = 2.64 \sigma_R^2 \Lambda^{5/6} \left[1 - {}_1F_1\left(-\frac{5}{6}; 1; \frac{2r^2}{W^2}\right)\right], \quad (18)$$

where ${}_1F_1(a; c; x)$ is the confluent hypergeometric function (see Appendix I). The corresponding expression for the longitudinal component (17) is [2–4]

$$\sigma_{I,l}^2(L) = 3.86 \sigma_R^2 \operatorname{Re} \left[i^{5/6} {}_2F_1\left(-\frac{5}{6}, \frac{11}{6}; \frac{17}{6}; \bar{\Theta} + i\Lambda\right) - \frac{11}{16} \Lambda^{5/6} \right], \quad (19)$$

where ${}_2F_1(a, b; c; x)$ is the hypergeometric function of Gauss (see Appendix I). The quantity $\sigma_R^2 = 1.23 C_n^2 k^{7/6} L^{11/6}$, called the *Rytov variance* for a plane wave [see (20) below], is widely used as a measure of the strength of the scintillations. For example, we generally characterize weak irradiance fluctuations by the condition $\sigma_R^2 \ll 1$. Observe that in the limiting cases of a plane wave ($\bar{\Theta} = 1, \Lambda = 0$) and a spherical wave ($\bar{\Theta} = \Lambda = 0$), the radial term (18) vanishes

and the longitudinal term (19) reduces, respectively, to the well-known results [3]:

$$\begin{aligned}\sigma_{I,\text{pl}}^2(L) &= \sigma_R^2 = 1.23 C_n^2 k^{7/6} L^{11/6} \quad (\text{plane wave}), \\ \sigma_{I,\text{sp}}^2(L) &= 0.4 \sigma_R^2 = 0.5 C_n^2 k^{7/6} L^{11/6} \quad (\text{spherical wave}).\end{aligned}\tag{20}$$

The notation $\beta_0^2 = 0.4 \sigma_R^2$, known as the *spherical wave Rytov variance*, is a commonly used symbol for the scintillation index of a spherical wave, i.e., $\sigma_{I,\text{sp}}^2(L) = \beta_0^2$. By combining (18) and (19), the general expression for the scintillation index (14) becomes

$$\begin{aligned}\sigma_I^2(\mathbf{r}, L) &= 3.86 \sigma_R^2 \text{Re} \left[i^{5/6} {}_2F_1 \left(-\frac{5}{6}, \frac{11}{6}; \frac{17}{6}; \bar{\Theta} + i\Lambda \right) \right] \\ &\quad - 2.64 \sigma_R^2 \Lambda^{5/6} {}_1F_1 \left(-\frac{5}{6}; 1; \frac{2r^2}{W^2} \right).\end{aligned}\tag{21}$$

In practice, it is generally useful to have simple analytic approximations for the scintillation index (21). Accurate approximations covering general Gaussian-beam waves have been developed for several spectral models [5] (see Tables VII through IX in Appendix III). For instance, based on the Kolmogorov spectrum, an approximation for the radial term (18) is

$$\sigma_{I,r}^2(\mathbf{r}, L) \cong 4.42 \sigma_R^2 \Lambda^{5/6} \frac{r^2}{W^2}, \quad r < W,\tag{22}$$

deduced from the small-argument asymptotic form of the confluent hypergeometric function. Coupled with an approximation for the longitudinal term in the case of a collimated or divergent beam, the total scintillation index can be closely approximated by the simple algebraic form

$$\begin{aligned}\sigma_I^2(\mathbf{r}, L) &\cong 4.42 \sigma_R^2 \Lambda^{5/6} \frac{r^2}{W^2} + 3.86 \sigma_R^2 \left\{ 0.40[(1 + 2\bar{\Theta})^2 + 4\Lambda^2]^{5/12} \right. \\ &\quad \times \cos \left[\frac{5}{6} \tan^{-1} \left(\frac{1 + 2\bar{\Theta}}{2\Lambda} \right) \right] - \frac{11}{16} \Lambda^{5/6} \left. \right\}, \quad r < W.\end{aligned}\tag{23}$$

In Fig. 8.1 we plot the scintillation index (21) [or (23)] along the optical axis (beam center at $r = 0$) and also at the diffractive beam edge ($r = W$) as a function of beam parameter Λ_0 . Off-axis scintillation is greatest for beam diameters comparable in size with the Fresnel zone (i.e., $\Lambda_0 \sim 1$), whereas in the near field ($\Lambda_0 \ll 1$) and far field ($\Lambda_0 \gg 1$) the off-axis scintillation diminishes.

The notion of weak fluctuations as described in Section 5.2 is based on the condition that the scintillation index satisfies $\sigma_I^2(\mathbf{r}, L) < 1$ at any point within the spot size of the beam. From Eq. (23), it follows that this inequality can always be satisfied within the diffraction-limited spot size of the beam (i.e., for

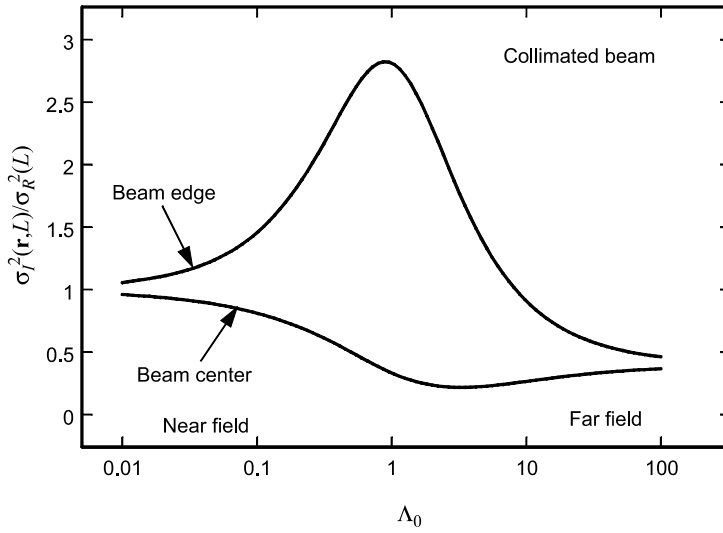


Figure 8.1 Scaled scintillation index for a collimated beam under weak irradiance fluctuations as a function of Fresnel parameter $\Lambda_0 = 2L/kW_0^2$.

$r < W$) by imposing the joint conditions $\sigma_R^2 \ll 1$ and $\sigma_R^2 \Lambda^{5/6} \ll 1$ prescribed in (16) of Chap. 5.

8.2.1 Inner scale models

The presence of a finite inner scale generally has a strong effect on the scintillation index, particularly under weak-to-moderate irradiance fluctuations. For example, a finite inner scale based on the modified atmospheric (or bump) spectrum leads to a corresponding bump in the scintillation index for certain values of the nondimensional parameter $Q_l = 10.89L/kl_0^2$ as compared with the traditional Tatarskii spectrum [6].

To develop analytic models of the scintillation index that produce results like those in Figs. 8.3–8.7 below, we will illustrate an approach using the infinite plane wave model described by Eq. (17) with $\Theta = 1$ and $\Lambda = 0$, viz.,

$$\sigma_{I,pl}^2(L) = 8\pi^2 k^2 L \int_0^1 \int_0^\infty \kappa \Phi_n(\kappa) \left[1 - \cos\left(\frac{L\kappa^2 \xi}{k}\right) \right] d\kappa d\xi. \quad (24)$$

However, for the sake of mathematical simplicity, we illustrate the calculations here based on the von Kármán spectrum

$$\Phi_n(\kappa) = 0.033 C_n^2 \frac{\exp(-\kappa^2/\kappa_m^2)}{(\kappa^2 + \kappa_0^2)^{11/6}}, \quad \kappa_m = 5.92/l_0, \quad \kappa_0 = 2\pi/L_0. \quad (25)$$

If we write the cosine function in (24) as $\cos x = \text{Re}(e^{-ix})$ through use of Euler's formula, the substitution of (25) into (24) leads to

$$\begin{aligned} \sigma_{I,\text{pl}}^2(L) = & 2.61 C_n^2 k^2 L \text{Re} \int_0^1 \int_0^\infty \frac{\kappa}{(\kappa^2 + \kappa_0^2)^{11/6}} \\ & \times \left\{ \exp\left(-\frac{\kappa^2}{\kappa_m^2}\right) - \exp\left[-\frac{\kappa^2(1 + iQ_m\xi)}{\kappa_m^2}\right] \right\} d\kappa d\xi, \end{aligned} \quad (26)$$

where $Q_m = 35.05L/kl_0^2$. Next, the inside integration yields (integral #17 in Appendix II)

$$\begin{aligned} \sigma_{I,\text{pl}}^2(L) = & 1.30 C_n^2 k^2 L \text{Re} \int_0^1 \left\{ \frac{1}{\kappa_0^{5/3}} U\left(1; \frac{1}{6}; \frac{\kappa_0^2}{\kappa_m^2}\right) \right. \\ & \left. - \frac{1}{\kappa_0^{5/3}} U\left(1; \frac{1}{6}; \frac{\kappa_0^2(1 + iQ_m\xi)}{\kappa_m^2}\right) \right\} d\xi, \end{aligned} \quad (27)$$

where $U(a; c; x)$ is the confluent hypergeometric function of the second kind. Because $\kappa_0^2/\kappa_m^2 \sim l_0^2/L_0^2 \ll 1$, we can use the small-argument approximation of the confluent hypergeometric function given by (CH8) in Appendix I to reduce (27) to

$$\begin{aligned} \sigma_{I,\text{pl}}^2(L) = & 8.70 C_n^2 k^2 L \kappa_m^{-5/3} \text{Re} \int_0^1 [(1 + iQ_m\xi)^{5/6} - 1] d\xi \\ = & 8.70 C_n^2 k^2 L \kappa_m^{-5/3} \frac{6}{11} \text{Re} \left[\frac{(1 + iQ_m)^{11/6}}{iQ_m} - \frac{1}{iQ_m} - \frac{11}{6} \right]. \end{aligned} \quad (28)$$

By simplifying the last expression above, we are led to our general result

$$\sigma_{I,\text{pl}}^2(L) = 3.86 \sigma_R^2 \left[\left(1 + \frac{1}{Q_m^2}\right)^{11/12} \sin\left(\frac{11}{6} \tan^{-1} Q_m\right) - \frac{11}{6} Q_m^{-5/6} \right]. \quad (29)$$

Note in the above analysis that, although we introduced outer scale effects through the parameter κ_0 , this parameter has negligible effect on the resulting plane wave scintillation index (29) under weak fluctuation conditions. Also, if we allow the inner scale to vanish (i.e., let $Q_m \rightarrow \infty$), it is easy to see that Eq. (29) reduces to $\sigma_{I,\text{pl}}^2(L) = \sigma_R^2$.

Equation (29) is an exact result under the conditions cited in obtaining it. To derive similar expressions in the case of a spherical wave or Gaussian-beam wave, we find that we must resort to some additional approximations along the way. In the case of a Gaussian-beam wave, for example, it has been shown that

the scintillation index based on the von Kármán spectrum (25) leads to the approximation [5]

$$\begin{aligned} \sigma_I^2(r, L) = & 3.93 \sigma_R^2 \Lambda^{5/6} \left[\left(\frac{\Lambda Q_m}{1 + 0.52 \Lambda Q_m} \right)^{1/6} - 1.29 (\Lambda Q_0)^{1/6} \right] \frac{r^2}{W} \\ & + 3.86 \sigma_R^2 \left\{ 0.40 \frac{[(1 + 2\Theta)^2 + (2\Lambda + 3/Q_m)^2]^{11/12}}{[(1 + 2\Theta)^2 + 4\Lambda^2]^{1/2}} \sin\left(\frac{11}{6} \varphi_1 + \varphi_2\right) \right. \\ & \left. - \frac{6\Lambda}{Q_m^{11/6} [(1 + 2\Theta)^2 + 4\Lambda^2]} - \frac{11}{6} \left(\frac{1 + 0.31 \Lambda Q_m}{Q_m} \right)^{5/6} \right\}, \end{aligned} \quad (30)$$

where we retain outer scale effects ($Q_0 = L\kappa_0^2/k$) in the radial component and where

$$\varphi_1 = \tan^{-1} \left[\frac{(1 + 2\Theta)Q_m}{3 + 2\Lambda Q_m} \right], \quad \varphi_2 = \tan^{-1} \left(\frac{2\Lambda}{1 + 2\Theta} \right). \quad (31)$$

The plane wave expression (29) is a limiting case of (30) obtained by setting $\Theta = 1, \Lambda = 0$, and the corresponding expression for the limiting case of a spherical wave is readily deduced by setting $\Theta = \Lambda = 0$.

Comparable expressions for the scintillation index (for plane waves, spherical waves, and Gaussian-beam waves) based on the modified atmospheric spectrum are provided in Appendix III. In general, the required calculations in using this more general spectrum model are virtually the same as those encountered in using the von Kármán spectrum.

8.2.2 Numerical results

Inner scale plays a significant role in the scintillation index under weak fluctuations, but outer scale effects are insignificant for infinite plane waves and spherical waves in this regime. In Fig. 8.2 we plot the scintillation index of a spherical wave as a function of the spherical wave Rytov parameter $\beta_0 = (0.5C_n^2 k^{7/6} L^{11/6})^{1/2}$ and various values of the inner scale l_0 . The curve corresponding to $l_0 = 0$ is based on the Kolmogorov spectrum whereas the other curves corresponding to nonzero values of the inner scale are based on the modified atmospheric (bump) spectrum. Note that the predicted scintillation index for the larger inner scale values (viz., $l_0 = 5, 10$ mm) is less than that predicted by the Kolmogorov spectrum ($l_0 = 0$). This is a consequence of the behavior in the modified atmospheric spectrum as a function of inner scale. As a final point we remark that, although values of $\beta_0 > 1$ may suggest the onset of moderate-to-strong irradiance fluctuations, in some cases the scintillation index may still be less than unity.

Miller et al. [5] did a numerical study on the role of the spectrum model in predicting the scaled scintillation index $\sigma_I^2(\mathbf{r}, L)/\sigma_R^2$ of a Gaussian-beam wave. Some of these results are shown in Figs. 8.3 through 8.6 for various spectral

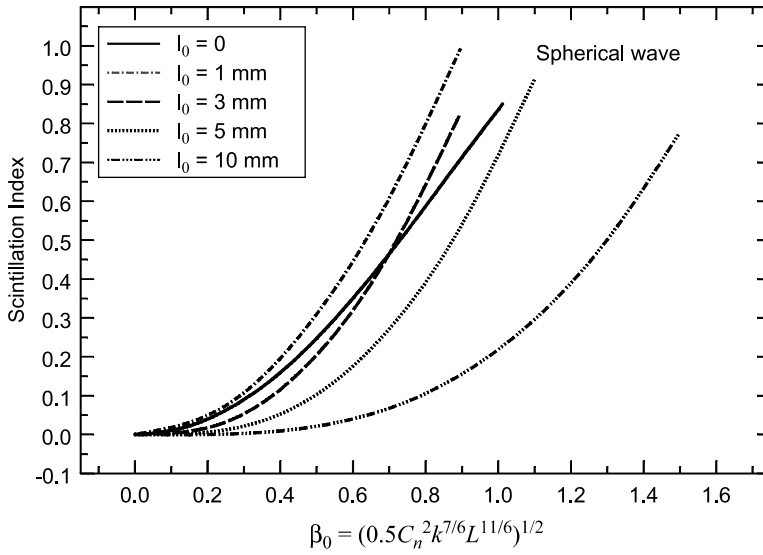


Figure 8.2 Scintillation index of a spherical wave as a function of turbulence strength β_0 and various values of the inner scale l_0 .

models discussed in Chap. 3. The path length and wavelength are fixed at $L = 250$ m and $\lambda = 1.06 \mu\text{m}$. In this fashion, all variations in the Fresnel ratio $\Lambda_0 = 2L/kW_0^2$ correspond to changes in the transmitter beam radius W_0 . Inner scale and outer scale values are assumed to be $l_0 = 3.9$ mm and $L_0 = 1.7$ m, typical of near-ground horizontal paths. The lower set of curves in each figure

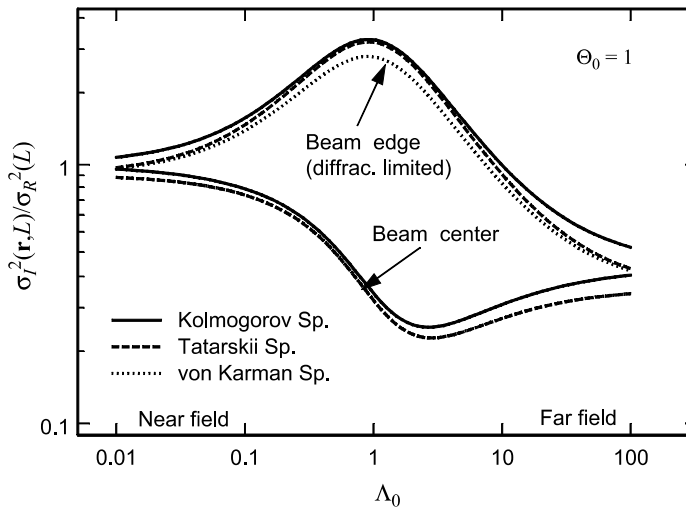


Figure 8.3 Scaled scintillation index for a collimated beam as a function of Λ_0 and various spectrum models. The path length is fixed at $L = 250$ m, inner scale at $l_0 = 3.9$ mm, and outer scale at $L_0 = 1.7$ m.

represents on-axis scintillations ($r = 0$) while the upper set of curves depicts scintillation levels at the diffraction-limited beam edge ($r = W$).

In Fig. 8.3, the Tatarskii spectrum [Eq. (19) in Chap. 3] and von Kármán spectrum [Eq. (20) in Chap. 3] predict essentially the same on-axis results, both showing scintillation levels lower than those predicted by the Kolmogorov spectrum. It can be shown in general that outer scale effects at the beam axis are not significant. At the diffraction-limited beam edge, however, all three spectral models predict vastly different values than those at the optical axis. Near $\Lambda_0 = 1$, where peak off-axis scintillation occurs, the Kolmogorov and Tatarskii models predict almost the same scintillation levels, indicating that inner scale effects based on the Tatarskii spectrum diminish near the beam edge for Λ_0 near unity. But, the von Kármán spectrum predicts decreased scintillation near this peak value, suggesting that outer scale effects significantly reduce off-axis scintillation levels for beam sizes in the range $0.1 < \Lambda_0 < 10$. In general, off-axis behavior transitions smoothly between $r = 0$ and $r = W$. Scintillation predicted by all models approaches that of an unbounded plane wave as $\Lambda_0 \rightarrow 0$ (near-field approximation) and that of a spherical wave as $\Lambda_0 \rightarrow \infty$ (far-field approximation).

Figure 8.4 includes the Kolmogorov spectrum results from Fig. 8.3 along with those based on the Hill numerical (bump) spectrum [6] and the modified atmospheric spectrum. It is well known that the presence of a spectral bump can produce enhanced scintillation for both plane and spherical wave propagation [6] (see also Fig. 8.2), and Fig. 8.4 shows it for a Gaussian-beam wave where the Hill spectrum and modified spectrum predict nearly the same on-axis results. Off-axis, the Hill spectrum also predicts greater scintillation levels than the Kolmogorov spectrum owing to the bump, but a marked distinction exists between results implied by the Hill model and modified atmospheric spectrum. This is clearly an outer scale effect because the Hill numerical spectrum involves only the inner scale parameter.¹

Figures 8.5 and 8.6 for a convergent beam ($\Theta_0 = 0.1$) are basically the same as Figs. 8.3 and 8.4 for a collimated beam. As before, outer scale effects become significant away from the beam centerline but seem to occur over a wider range of beam sizes than for the collimated beam case. In addition, outer scale effects near the diffraction-limited beam edge for $\Lambda_0 \sim 0.1$ are more pronounced than either inner scale or spectral bump.

8.3 Beam Wander and Scintillation

Results presented in Section 8.2 are based on first-order Rytov theory. However, in spite of the progress that has been made in developing these scintillation models, there are still some aspects of beam wave scintillation that are not well understood, particularly in regard to convergent and perfectly focused beams. For example, weak fluctuation theory predicts that the longitudinal component of a focused

¹When $\kappa_0 = 0$, the modified atmospheric spectrum and Hill numerical spectrum predict essentially the same on-axis and off-axis results.

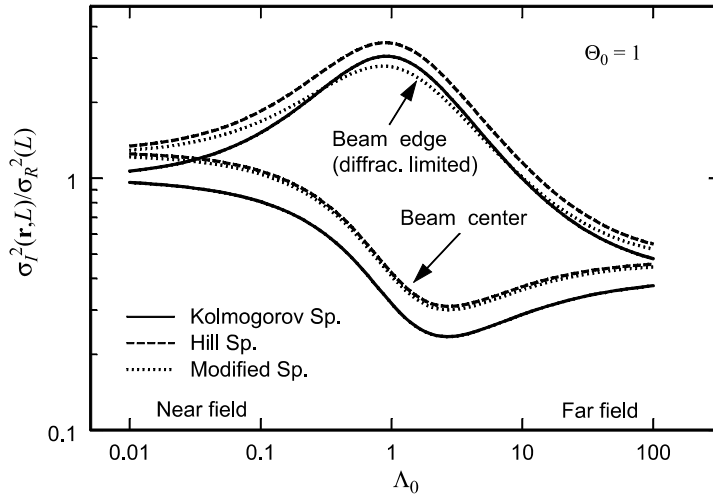


Figure 8.4 Same as Fig. 8.3 but for different spectrum models.

beam along a horizontal path continuously decreases as the size of the laser-transmitter aperture increases [2–5]. At the same time, the theory predicts that the radial component of scintillation increases without bound. Similar on-axis behavior has been predicted for a collimated beam on an uplink path through weak turbulence to a satellite [3,7,8] (see also Chap. 12). Because such behavior is physically unrealistic, we conclude that the first-order Rytov theory is incomplete with regard to these cases.

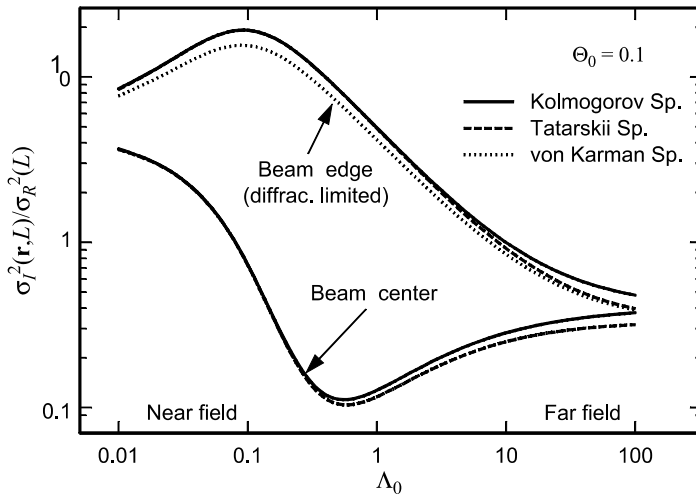


Figure 8.5 Scaled scintillation index for a convergent beam as a function of Λ_0 and various spectrum models. The path length is fixed at $L = 250$ m, the inner scale at $l_0 = 3.9$ mm, and the outer scale at $L_0 = 1.7$ m.

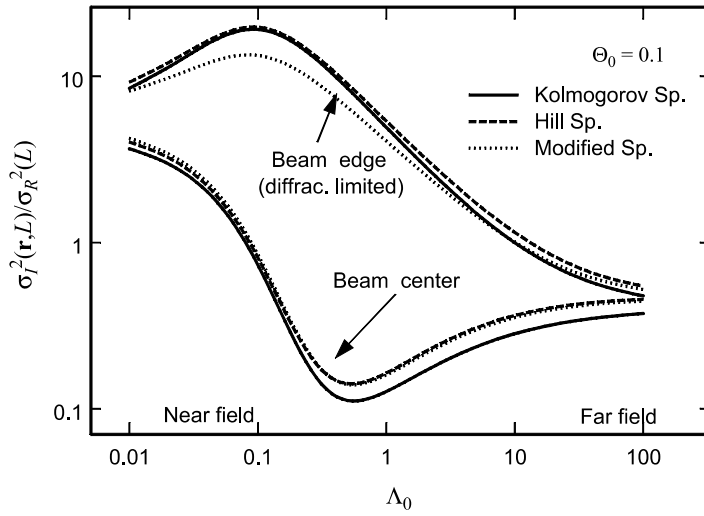


Figure 8.6 Same as Fig. 8.5 but for different spectrum models.

In an early experimental study, Kerr and Dunphy [9] deduced that the predicted on-axis scintillation reduction in the near field of a focused beam will not be realized in the presence of significant beam wander. Early theoretical studies addressing power reduction caused by beam wander include those of Esposito [10], Fried [11], and Titterton [12]. These particular studies were concerned with developing a probability density function (PDF) model to describe the statistics of pointing jitter in the absence of atmospheric turbulence. More recently, Kiasaleh [13] and Steinvall [14] examined the impact of pointing jitter combined with beam scintillation on the irradiance PDF, employing several PDF models for irradiance fluctuations. Concern with the Rytov theory for focused beams has also been expressed by others such as Banakh and Smalikho [15]. However, none of these studies produced a consistent, tractable model of scintillation that combines beam wander effects with conventional scintillation theory.

The relation between the *long-term spot size* W_{LT} , the *short-term spot size* W_{ST} , and the *beam wander variance* of a Gaussian-beam wave is given by (see Section 6.6)

$$W_{LT}^2 = W^2 + W^2 T_{SS} + \langle r_c^2 \rangle = W_{ST}^2 + \langle r_c^2 \rangle, \quad (32)$$

where SS denotes small scale. The long-term spot size W_{LT} arises from the effects of turbulent cells or “eddies” of all scale sizes. Turbulent eddies larger than the beam diameter lead to refractive effects known as beam wander and are described by the variance $\langle r_c^2 \rangle$ of the random displacement of the instantaneous center of the short-term spot size. Turbulent scale sizes smaller than the beam diameter produce diffractive effects that lead to “beam breathing” described by $W^2 T_{SS}$.

It was shown many years ago that the *principle of reciprocity* applies to the performance of a telescope as measured by its effective coherence size in atmospheric turbulence, whether it is functioning as part of a transmitter or as part of a receiver

[16]. Thus, by invoking the reciprocity principle, we argue that beam wander at the receiver plane can be modeled as if it arises from a random wave front tilt at the transmitter plane, equal to that of a reciprocal propagating wave with transmitter aperture replacing the receiver aperture [e.g., see Eqs. (84) and (95) in Chap. 6].

For interpretation purposes, it is useful to write the rms beam wander displacement of a collimated beam in the form

$$\sqrt{\langle r_c^2 \rangle} = 0.69 L \left(\frac{\lambda}{2W_0} \right) \left(\frac{2W_0}{r_0} \right)^{5/6}, \quad (33)$$

where $\lambda/2W_0$ is the diffraction angle of the transmitted beam and $r_0 = (0.16C_n^2 k^2 L)^{-3/5}$ is *Fried's parameter*, or *atmospheric coherence width* (see Chap. 14), of a reciprocal propagating point source from the receiver at distance L . Only the constant is different for a focused beam. Beam wander therefore arises largely from tilt phase fluctuations averaged over the transmitter aperture on the order of $(2W_0/r_0)^{5/3}$.

Beam wander describes “dancing” of the instantaneous center (“hot spot”) of the beam caused by large random inhomogeneities whose size is bounded above by the outer scale L_0 [see (97) in Chap. 6]. Similarly, we define *beam jitter* as the whole short-term beam moving around its unperturbed position in the receiver plane. Because it is caused by random inhomogeneities bounded above by r_0 ($r_0 \ll L_0$), beam jitter acts like an effective wave front tilt at the transmitter that can be significantly smaller than the wave front tilt associated with the hot spot dancing. Recalling Fig. 6.7, the total beam wander (including hot spot dancing and beam jitter) causes a widening of the long-term beam profile near the boresight that leads to a slightly “flattened” beam as depicted below in Fig. 8.7(a). The dashed curves in the figure represent a conventional Gaussian-beam profile as suggested by Rytov theory. Consequently, the short-term beam jitter creates a “beam center” defined across the flattened portion at the beam axis, corresponding to the area within the circumference of the lightly-shaded circle with radius σ_{pe} shown in Fig. 8.7(b). For the untracked beam case the net result of the flattened beam profile is an “effective pointing error” σ_{pe} that creates an increase in the longitudinal scintillation index that is not accounted for in the first-order Rytov theory.

For beams in which $2W_0 < r_0$, scintillation caused by short-term pointing jitter is the result of turbulent cells near the transmitter on the order of the beam diameter and larger up to the atmospheric coherence width r_0 . Hence, analogous to the beam wander model developed in Section 6.6, we introduce the spatial frequency filter function

$$H(\kappa, \xi)_{\text{jitter}} = \exp[-\kappa^2 W_0^2 (\Theta_0 + \bar{\Theta}_0 \xi)^2] \left[1 - \exp\left(-\frac{\kappa^2}{\kappa_r^2}\right) \right], \quad (34)$$

where $\xi = 1 - z/L$ and

$$\kappa_r = \frac{C_r}{r_0}. \quad (35)$$

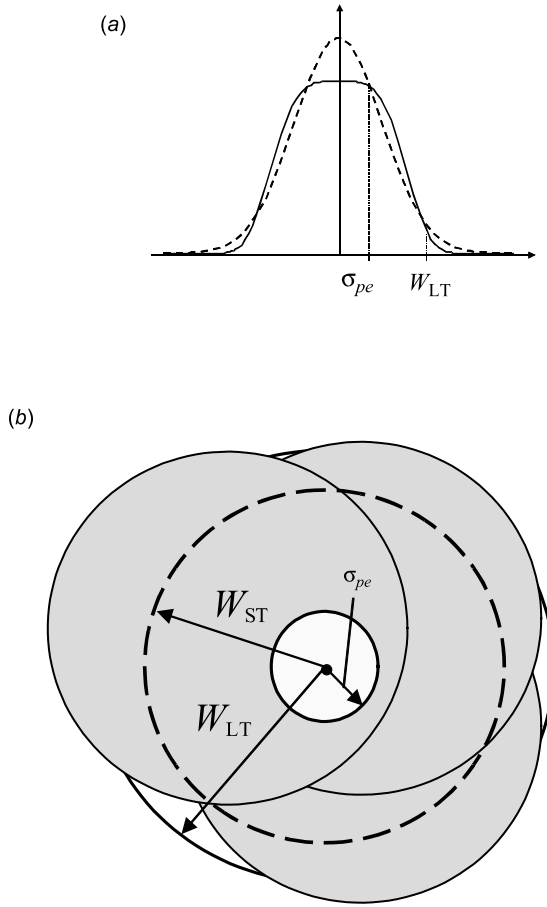


Figure 8.7 (a) Beam profile for the untracked beam as a function of radial distance. (b) The small circle in the center describes the effective rms pointing error of the beam and the dashed circle denotes the rms short-term beam spot size.

The parameter C_r is a scaling constant typically on the order $C_r \sim 2\pi$. When $2W_0 \geq r_0$, the same filter function is also used, but in this case the amplitude of the filter tends to zero as the coherence width r_0 diminishes.

To calculate the jitter-induced *pointing error variance* σ_{pe}^2 , we substitute the filter function (34) into the integral in (38) in Chap. 6 multiplied by W^2 to find

$$\begin{aligned} \sigma_{pe}^2 &= 4\pi^2 k^2 L W^2 \int_0^1 \int_0^\infty \kappa \Phi_n(\kappa) H(\kappa, \xi)_{\text{jitter}} (1 - e^{-\Lambda L \kappa^2 \xi^2 / k}) d\kappa d\xi \\ &\cong 7.25 C_n^2 L^3 W_0^{-1/3} \int_0^1 \xi^2 \left\{ \frac{1}{|\Theta_0 + \bar{\Theta}_0 \xi|^{1/3}} - \left[\frac{\kappa_r^2 W_0^2}{1 + \kappa_r^2 W_0^2 (\Theta_0 + \bar{\Theta}_0 \xi)^2} \right]^{1/6} \right\} d\xi, \end{aligned} \quad (36)$$

where we have once again used the approximation $1 - \exp(-\Lambda L \kappa^2 \xi^2/k) \cong \Lambda L \kappa^2 \xi^2/k$ (see Section 6.6). Equation (36) in the case of a collimated beam ($\Theta_0 = 1$) yields

Collimated beam:

$$\sigma_{pe}^2 = 0.48 \left(\frac{\lambda L}{2W_0} \right)^2 \left(\frac{2W_0}{r_0} \right)^{5/3} \left[1 - \left(\frac{C_r^2 W_0^2 / r_0^2}{1 + C_r^2 W_0^2 / r_0^2} \right)^{1/6} \right], \quad (37)$$

and, for a focused beam ($\Theta_0 = 0$), the comparable expression is

Focused beam:

$$\sigma_{pe}^2 \cong 0.54 \left(\frac{\lambda L}{2W_0} \right)^2 \left(\frac{2W_0}{r_0} \right)^{5/3} \left[1 - \frac{8}{9} \left(\frac{C_r^2 W_0^2 / r_0^2}{1 + 0.5 C_r^2 W_0^2 / r_0^2} \right)^{1/6} \right]. \quad (38)$$

Depending on the value of the ratio $2W_0/r_0$, we can easily deduce the asymptotic behavior given by

$$\sigma_{pe}^2 \sim \begin{cases} \left(\frac{\lambda L}{2W_0} \right)^2 \left(\frac{2W_0}{r_0} \right)^{5/3}, & 2W_0/r_0 \ll 1 \\ \left(\frac{\lambda L}{2W_0} \right)^2 \left(\frac{r_0}{2W_0} \right)^{1/3}, & 2W_0/r_0 \gg 1. \end{cases} \quad (39)$$

Expressions (39) apply for both collimated and focused beams. As a consequence, even though there can be significant beam wander in some cases (i.e., with small beams), the related pointing error variance (39) in both asymptotic cases will tend to zero.

8.3.1 Untracked beam

Although beam wander effects are contained in the on-axis behavior of the irradiance through the long-term spot radius, this is not the case for the on-axis irradiance *normalized* by its mean value, i.e., $\hat{I}(0, L) = I(0, L)/\langle I(0, L) \rangle$. As a consequence, beam wander effects are not included in any on-axis moments of the normalized irradiance $\langle \hat{I}^n \rangle$, $n = 1, 2, 3, \dots$, which relates to the scintillation index $\sigma_I^2(0, L) = \langle \hat{I}^2(0, L) \rangle - 1$. We therefore deduce that the longitudinal component of the scintillation index (19) describes irradiance fluctuations only in the absence of any beam-wander-induced pointing error.

In view of the above comments, we need to redefine the components of the scintillation index, depending on whether the beam is tracked or not. Because σ_{pe} represents an apparent pointing error displacement of a Gaussian beam at the receiver, we define the *longitudinal component* for an *untracked beam* by the expression

$$\begin{aligned} \sigma_{I, l}^2(L)_{\text{untracked}} &= 4.42 \sigma_R^2 \Lambda^{5/6} \left(\frac{\sigma_{pe}}{W} \right)^2 \\ &+ 3.86 \sigma_R^2 \text{Re} \left[i^{5/6} {}_2F_1 \left(-\frac{5}{6}, \frac{11}{6}; \frac{17}{6}; \bar{\Theta} + i\Lambda \right) - \frac{11}{16} \Lambda^{5/6} \right]. \end{aligned} \quad (40)$$

The first term on the right-hand side, which arises from the wander-induced pointing error, is simply the conventional radial term for the scintillation index (22) evaluated at the rms error displacement $r = \sigma_{pe}$. In the case of a collimated beam, we have $\Lambda \leq 0.5$ and the ratio σ_{pe}^2/W^2 will generally be small for all aperture sizes. Hence, there should be little effect from wander-induced pointing errors. For a focused beam, however, the free-space spot radius W will decrease significantly with increasing aperture radius causing Λ to increase. Thus, even with little change in the ratio σ_{pe}^2/W^2 , the pointing error term in (40) for a large focused beam can lead to fairly large scintillation values. To also include radial distances $r > \sigma_{pe}$, we define the scintillation index throughout the beam profile by

$$\sigma_{I,l}^2(\mathbf{r}, L)_{\text{untracked}} = 4.42 \sigma_R^2 \Lambda^{5/6} \left(\frac{r - \sigma_{pe}}{W} \right)^2 U(r - \sigma_{pe}) + \sigma_{I,l}^2(L)_{\text{untracked}}, \quad (41)$$

where $0 \leq r < W$ and $U(x)$ is the unit step function defined by

$$U(x) = \begin{cases} 1, & x > 0 \\ 0, & x < 0. \end{cases} \quad (42)$$

Although the true behavior of the scintillation index across the beam profile is not that of a step function, it is convenient in our model of pointing-error-induced scintillation to use the step function and assume that the off-axis scintillation (41) is equal to the longitudinal component throughout the circular domain $0 \leq r \leq \sigma_{pe}$.

8.3.2 Tracked beam

The methods of “tracking a beam” can vary from system to system. In general, it might mean tracking the hot spot in the beam (point of maximum irradiance) or removing wave front tilt, among other methods. Theoretical results for tracked beams are therefore dependent on the tracking technique. For the model developed below we define a *tracked beam* as one based on eliminating all beam wander effects, which for constant C_n^2 , is similar to removing the rms wave front tilt. Thus, the tracked beam in this model acts like it has a “flattened” irradiance profile near the optical axis out to the rms beam wander displacement radius, resulting in a nearly constant scintillation index throughout a disk in the center portion of the beam.

Because beam wander effects are not included in the conventional first-order Rytov theory for on-axis scintillation, we assume for a tracked beam it leads to the correct result for the *longitudinal component* of the scintillation index, viz.,

$$\sigma_{I,l}^2(L)_{\text{tracked}} = 3.86 \sigma_R^2 \text{Re} \left[i^{5/6} {}_2F_1 \left(-\frac{5}{6}, \frac{11}{6}; \frac{17}{6}; \bar{\Theta} + i\Lambda \right) - \frac{11}{16} \Lambda^{5/6} \right]. \quad (43)$$

However, the removal of beam wander through perfect tracking yields a result at off-axis positions that does not agree with conventional Rytov theory. In particular, the removal of the rms beam wander displacement from the radial component

leads to smaller values of the scintillation index at off-axis points than predicted by first-order Rytov theory. We remove beam wander by the formal replacement of r with $r - \sqrt{\langle r_c^2 \rangle}$ in the radial term (22) to find

$$\begin{aligned} \sigma_I^2(\mathbf{r}, L)_{\text{tracked}} = & 4.42 \sigma_R^2 \Lambda^{5/6} \left(\frac{r - \sqrt{\langle r_c^2 \rangle}}{W} \right)^2 U \left(r - \sqrt{\langle r_c^2 \rangle} \right) + 3.86 \sigma_R^2 \\ & \times \operatorname{Re} \left[i^{5/6} {}_2F_1 \left(-\frac{5}{6}, \frac{11}{6}; \frac{17}{16}; \overline{\Theta} + i\Lambda \right) - \frac{11}{16} \Lambda^{5/6} \right], \end{aligned} \quad (44)$$

where $0 \leq r < W$. Note that in (44) the change of scintillation index in the radial direction does not occur until r exceeds the rms beam wander displacement. However, the validity of (43) and (44) for large-aperture focused beams is still under investigation.

In Fig. 8.8 we illustrate the effect of beam-wander-induced scintillation associated with a collimated beam propagating over a 1 km path through weak irradiance fluctuations. We set $\lambda = 1.55 \mu\text{m}$ and $C_n^2 = 10^{-14} \text{ m}^{-2/3}$ in Fig. 8.8 and use the above results (40), (41), (43), and (44), all based on a Kolmogorov spectrum. The solid curves correspond to (40) and (41) for the untracked beam, whereas the dashed curves represent that predicted on-axis by (43) and that at $r = W$ (off-axis) by (44) for the case when beam wander is removed (i.e., the beam is perfectly tracked).

In Fig. 8.9 we present simulation results for tracked and untracked beams along with theoretical results over a 10 km path and $C_n^2 = 1.39 \times 10^{-16} \text{ m}^{-2/3}$. Analogous to the theoretical curves, the simulation results show very little

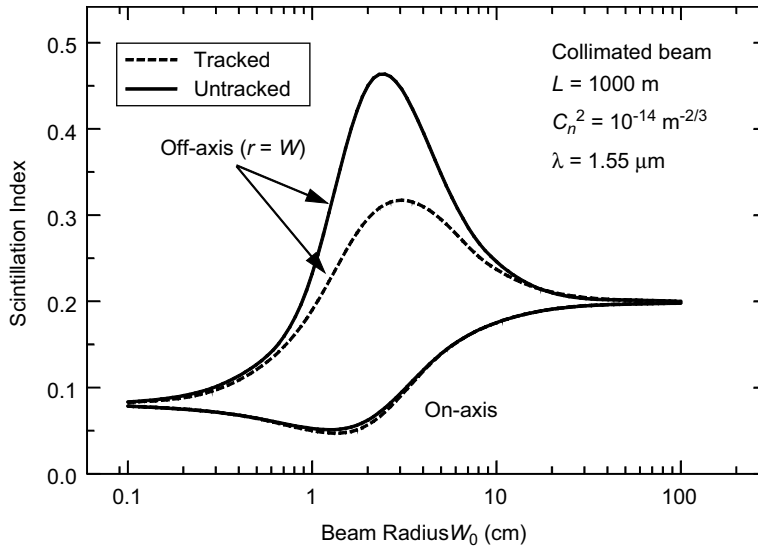


Figure 8.8 Theoretical curves for the scintillation index of a collimated beam over a 1 km path as a function of beam spot radius at the transmitter. Both tracked and untracked cases are illustrated.

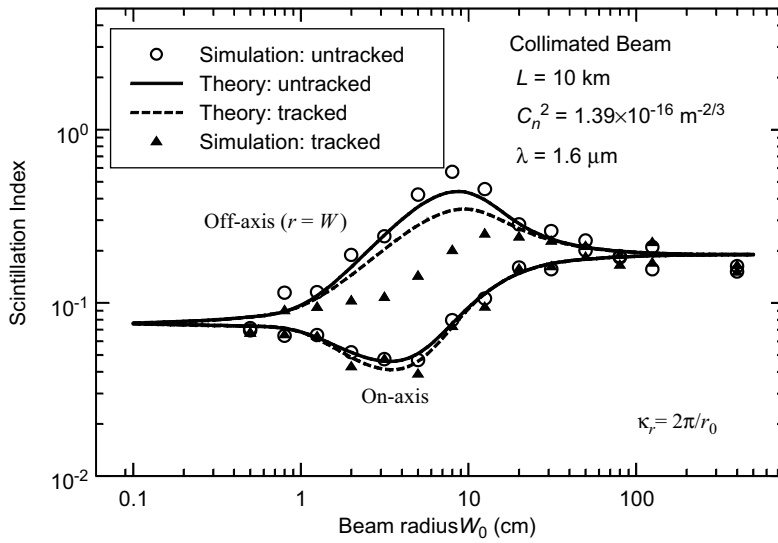


Figure 8.9 Simulation results and theoretical curves for both tracked and untracked collimated beam over a 10 km path. (Simulation results courtesy of G. J. Baker.)

change in the on-axis scintillation index between the tracked and untracked cases. That is, even though the rms beam wander displacement in this case is on the order of 2–4 cm, the effect of the apparent pointing error on the longitudinal component of scintillation is negligible. Moreover, it can be shown that the scintillation index deduced from conventional Rytov theory is applicable throughout the beam profile in the case of an untracked collimated beam propagating along a horizontal path. In the case of a tracked beam, however, the situation is different at off-axis positions. In particular, we see that tracking a beam can lead to reduced scintillation at points away from the apparent center of the beam. And, although the beam wander theory shows good agreement with the simulation results for the untracked beam, the theoretical curve for the tracked beam case predicts off-axis scintillation values that are generally larger than corresponding simulation results. This is a consequence of comparing different tracking techniques—i.e., the center of the beam was moved to the boresight in each realization of the simulation results before averaging. Therefore, the simulation procedure can produce somewhat different scintillation values after averaging than that obtained by first averaging and then removing the rms beam wander displacement.

We illustrate similar cases in Figs. 8.10 and 8.11 for a beam focused at the receiver. Theoretical results for both tracked and untracked beams are shown in Fig. 8.10 and simulation results for the untracked focused beam are shown in Fig. 8.11 along with theoretical models. The first-order Rytov theory predicts a strong reduction in the on-axis scintillation as the transmitter beam radius increases [dashed curve in Fig. 8.10]. However, this may be possible only if all beam wander effects are completely eliminated, which in general is difficult or impossible to do. For the untracked beam, the large reduction in on-axis

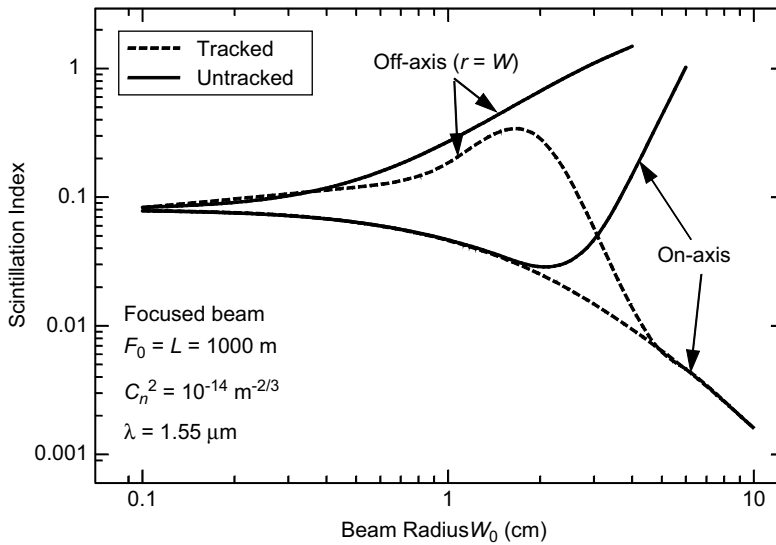


Figure 8.10 Same as Fig. 8.8 except for a focused beam.

scintillation associated with a large-diameter tracked beam does not happen. Namely, for the untracked beam there is a minimal amount of scintillation reduction for moderate-sized beams and, for larger beams, the beam-jitter-induced on-axis scintillation begins to increase with increasing beam diameter and can eventually approach saturation as the transmitted beam size continues to grow.

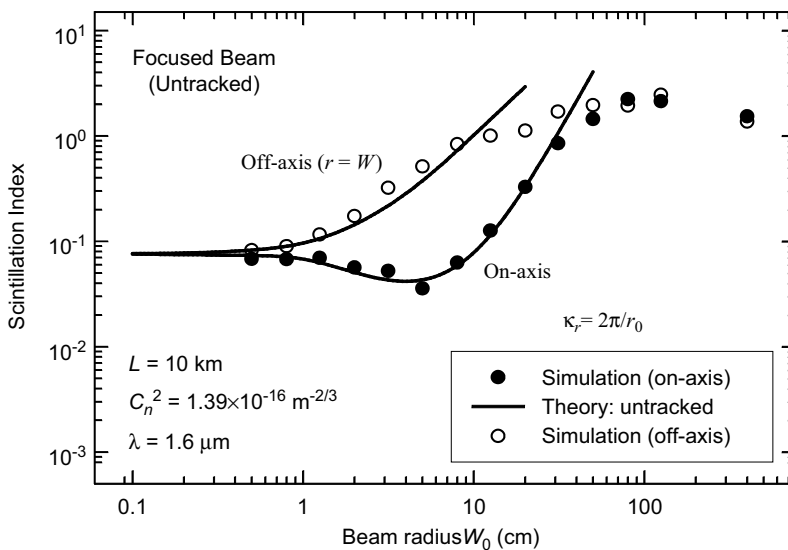


Figure 8.11 Same as Fig. 8.9 except for an untracked focused beam. (Simulation results courtesy of G. J. Baker.)

Finally, in the simulation results shown in Fig. 8.11, both the on-axis ($r = 0$) and off-axis ($r = W$) scintillation values approach saturation as the transmitter beam size increases. Because the corresponding theoretical results (solid curves) are based on weak irradiance fluctuations, they are valid on-axis only for beam radii of 20 cm or less and off-axis only for beam radii of 10 cm or less. In Section 12.6 we will show a similar trend of simulation results for the case of an untracked uplink collimated beam to space.

8.4 Covariance Function of Irradiance

In addition to the scintillation index, which describes irradiance fluctuations at a single point in the receiver plane, it is also useful to know how the irradiance fluctuations at one point in the beam are correlated with those at another point. Such a relation is described by the covariance function of irradiance.

To begin, we note that given two points \mathbf{r}_1 and \mathbf{r}_2 in the plane of the receiver, the *log-amplitude covariance* associated with a Gaussian-beam wave is obtained from the relation

$$\begin{aligned} B_\chi(\mathbf{r}_1, \mathbf{r}_2, L) &= \langle \chi_1(\mathbf{r}_1, L) \chi_1(\mathbf{r}_2, L) \rangle - \langle \chi_1(\mathbf{r}_1, L) \rangle \langle \chi_1(\mathbf{r}_2, L) \rangle \\ &= \frac{1}{2} \text{Re}[E_2(\mathbf{r}_1, \mathbf{r}_2) + E_3(\mathbf{r}_1, \mathbf{r}_2)], \end{aligned} \quad (45)$$

which depends on only the first-order log-amplitude perturbation and where we have retained terms of second order or less. Similar to the scintillation index, the *covariance function of irradiance fluctuations* under weak fluctuation theory can be approximated by $B_I(\mathbf{r}_1, \mathbf{r}_2, L) = 4B_\chi(\mathbf{r}_1, \mathbf{r}_2, L)$, which for homogeneous and isotropic turbulence leads to

$$\begin{aligned} B_I(\mathbf{p}, \mathbf{r}, L) &= 8\pi^2 k^2 L \int_0^1 \int_0^\infty \kappa \Phi_n(\kappa) \exp\left(-\frac{\Lambda L \xi^2 \kappa^2}{k}\right) \\ &\quad \times \text{Re} \left\{ J_0[\kappa|(1 - \bar{\Theta}\xi)\mathbf{p} - 2i\Lambda\xi\mathbf{r}|] \right. \\ &\quad \left. - \exp\left[-\frac{iL\kappa^2}{k}\xi(1 - \bar{\Theta}\xi)\right] J_0[(1 - \bar{\Theta}\xi - i\Lambda\xi)\kappa\rho] \right\} d\kappa d\xi, \end{aligned} \quad (46)$$

where we have introduced the following notation

$$\mathbf{r} = \frac{1}{2}(\mathbf{r}_1 + \mathbf{r}_2), \quad \mathbf{p} = \mathbf{r}_1 - \mathbf{r}_2, \quad \rho = |\mathbf{p}|. \quad (47)$$

Like the mutual coherence function (Chap. 6), the covariance function (46) is statistically inhomogeneous in that it depends on the location of the two points \mathbf{r}_1 and \mathbf{r}_2 within the beam. Note that for $\mathbf{r}_1 = \mathbf{r}_2 = \mathbf{r}$, the covariance function (46) reduces to the scintillation index (14). That is, the covariance function is a more general statistic that includes the scintillation index as a special case.

Because of the complexity of Eq. (46), we first consider the limiting cases of an infinite plane wave and a spherical wave, or point source. For an infinite plane wave ($\Theta = 1$, $\Lambda = 0$), Eq. (46) simplifies to [17]

$$\begin{aligned} B_{I,pl}(\rho, L) &= 8\pi^2 k^2 L \int_0^1 \int_0^\infty \kappa \Phi_n(\kappa) J_0(\kappa \rho) \left[1 - \cos\left(\frac{L\kappa^2 \xi}{k}\right) \right] d\kappa d\xi \\ &= 3.86 \sigma_R^2 \text{Im} \left[i^{1/6} {}_1F_1\left(-\frac{11}{6}; 1; -\frac{ik\rho^2}{4L}\right) \right] - 7.52 \sigma_R^2 \left(\frac{k\rho^2}{4L}\right)^{5/6}, \end{aligned} \quad (48)$$

where Im denotes the imaginary part of the argument. In arriving at the second line in (48), we have once again used the Kolmogorov power-law spectrum. Similarly, for a spherical wave ($\Theta = \Lambda = 0$), we find [18]

$$\begin{aligned} B_{I,sp}(\rho, L) &= 8\pi^2 k^2 L \int_0^1 \int_0^\infty \kappa \Phi_n(\kappa) J_0(\kappa \xi \rho) \left\{ 1 - \cos\left[\frac{L\kappa^2}{k} \xi(1 - \xi)\right] \right\} d\kappa d\xi \\ &= 3.86 \beta_0^2 \text{Re} \left[i^{5/6} {}_1F_1\left(\frac{11}{6}; 1; -\frac{ik\rho^2}{4L}\right) - 1.81 \left(\frac{k\rho^2}{4L}\right)^{5/6} \right] \\ &\quad - 5.54 \beta_0^2 \left(\frac{k\rho^2}{4L}\right)^{11/6} \text{Im} \left[{}_2F_2\left(\frac{11}{3}, 1; \frac{17}{6}, \frac{17}{6}; -\frac{ik\rho^2}{4L}\right) - 1 \right]. \end{aligned} \quad (49)$$

Although both (48) and (49) are exact results for these limiting cases, we will derive an approximation below for the Gaussian-beam wave from which we can deduce alternate forms for (48) and (49). For some of our later calculations, we find these alternate (approximate) forms to be more useful.

In the case of a general Gaussian-beam wave, an exact result for the covariance function (46) based on a Kolmogorov spectrum has not yet been derived. However, it can be closely approximated by (see Section 15.4)

$$\begin{aligned} B_I(\mathbf{p}, \mathbf{r}, L) &= 3.87 \sigma_R^2 \text{Re} \left\{ i^{5/6} [1 - (\bar{\Theta} + i\Lambda)d_t]^{5/6} \right. \\ &\quad \times {}_1F_1 \left[-\frac{5}{6}; 1; -\frac{(1 - \bar{\Theta}d_t - i\Lambda d_t)k\rho^2}{4iLd_t} \right] \\ &\quad \left. - (\Lambda d_t)^{5/6} {}_1F_1 \left[-\frac{5}{6}; 1; -\frac{k|(1 - \bar{\Theta}d_t)\mathbf{p} - 2i\Lambda d_t \mathbf{r}|^2}{4L\Lambda d_t^2} \right] \right\}, \end{aligned} \quad (50)$$

where $d_t = 0.67 - 0.17\Theta$. From (50), we can readily obtain the limiting plane wave and spherical wave approximations

$$B_{I,pl}(\rho, L) = 3.87 \sigma_R^2 \text{Re} \left[i^{5/6} {}_1F_1\left(-\frac{5}{6}; 1; \frac{ik\rho^2}{2L}\right) - 0.60 \left(\frac{k\rho^2}{L}\right)^{5/6} \right], \quad (51)$$

$$B_{I,\text{sp}}(\rho, L) = 3.87 \sigma_R^2 \text{Re} \left[0.40 i^{5/6} {}_1F_1 \left(-\frac{5}{6}; 1; \frac{ik\rho^2}{8L} \right) - 0.075 \left(\frac{k\rho^2}{L} \right)^{5/6} \right]. \quad (52)$$

The covariance function is useful in defining a characteristic *correlation width* ρ_c associated with irradiance fluctuations. This usually involves either the zero crossing point or the $1/e^2$ point of the *normalized covariance function* defined by ($\mathbf{r}_1 = -\mathbf{r}_2$)

$$b_I(\rho, L) = \frac{B_I(\rho, L)}{B_I(0, L)}. \quad (53)$$

Knowledge of the correlation width is useful in the choice of aperture size in a receiver system. That is, aperture sizes on the order of the correlation width ρ_c or smaller will act like a “point receiver.” Aperture sizes larger than ρ_c can lead to an important reduction in scintillation known as *aperture averaging* (see Chap. 10).

Graphs of Eq. (53) deduced from (50) are shown in Fig. 8.12 for various collimated beams. The case $\Lambda_0 = 0.01$ is similar to that for a plane wave and $\Lambda_0 = 100$ is similar to that for a spherical wave. Note that the correlation width is directly related to the size of the first Fresnel zone $\sqrt{L/k}$. In particular, the correlation width is smallest for the collimated beam characterized by $\Lambda_0 = 1$ [i.e., $\rho_c \sim \sqrt{L/k}$], and largest for the beam characterized by $\Lambda_0 = 100$ [i.e., $\rho_c \sim 3\sqrt{L/k}$]. The negative tail in all cases denotes separation distances in which, on the average, one of the observation points is in a bright region of the beam and the other observation point is in a dark region. Experimental confirmation of these results performed many years ago has more recently been summarized in Wheelon [19].

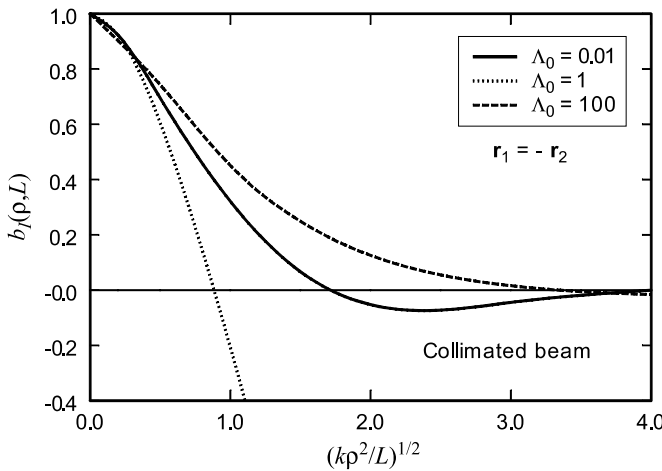


Figure 8.12 Normalized covariance function for three collimated Gaussian-beam waves as a function of $(k\rho^2/L)^{1/2}$. All results are based on the Kolmogorov spectrum.

8.5 Temporal Spectrum of Irradiance

The theory developed thus far has described optical turbulence in terms of *spatial statistics*. In most applications, however, the *temporal statistics* are actually measured. For this reason, the relation between temporal and spatial statistics is a central issue in any atmospheric measurements. In Section 3.4 we briefly discussed the *Taylor frozen turbulence hypothesis*, which permits converting spatial statistics into temporal statistics by knowledge of the average wind speed transverse to the direction of observation. Here, we wish to further pursue this approach in connection with the temporal spectrum of the irradiance fluctuations associated with a Gaussian-beam wave.

The temporal spectrum of the irradiance fluctuations resulting from the propagation of an optical wave through a random medium is one of the main characteristics of atmospheric noise associated with optical communication systems and laser radar systems. Following Tatarskii [20] and Ishimaru [3], the *temporal spectrum* of irradiance fluctuations, or *power spectral density* (PSD) $S_I(\omega)$, is defined by the Fourier transform of the temporal covariance function according to

$$S_I(\omega) = 2 \int_{-\infty}^{\infty} B_I(\tau, L) e^{-i\omega\tau} d\tau = 4 \int_0^{\infty} B_I(\tau, L) \cos(\omega\tau) d\tau, \quad (54)$$

where $B_I(\tau, L)$ is the temporal covariance function. The extra factor 2 in the transform integral is a consequence of considering only positive frequencies. From transform relations given in Chap. 2, it follows that the inverse transform yields

$$B_I(\tau, L) = \frac{1}{2\pi} \int_0^{\infty} S_I(\omega) \cos(\omega\tau) d\omega. \quad (55)$$

8.5.1 Plane wave

Based on either Eq. (48) or (51) for the covariance function associated with an unbounded plane wave, the frozen turbulence hypothesis allows us to make the association $\mathbf{p} = \mathbf{V}_{\perp} \tau$, where \mathbf{V}_{\perp} is the mean transverse wind velocity. Of course, we are tacitly assuming the mean transverse wind velocity is the same all along the propagation path. In the case of (51) for the spatial covariance function, the temporal covariance function (based on a Kolmogorov spectrum) takes the form

$$\begin{aligned} B_{I, \text{pl}}(\tau, L) &= 8\pi^2 k^2 L \int_0^1 \int_0^{\infty} \kappa \Phi_n(\kappa) J_0(\kappa V_{\perp} \tau) \left[1 - \cos\left(\frac{L \kappa^2 \xi}{k}\right) \right] d\kappa d\xi \\ &\cong 3.87 \sigma_R^2 \text{Re} \left[i^{5/6} {}_1F_1\left(-\frac{5}{6}; 1; \frac{ik V_{\perp}^2 \tau^2}{2L}\right) - 0.60 \left(\frac{k V_{\perp}^2 \tau^2}{L}\right)^{5/6} \right]. \end{aligned} \quad (56)$$

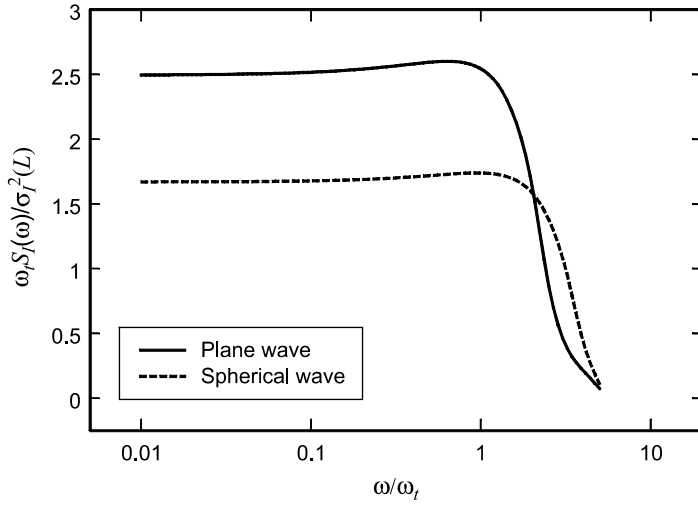


Figure 8.13 PSD of irradiance fluctuations scaled by the scintillation index and multiplied by $\omega_t = V_\perp / \sqrt{L/k}$.

If we substitute (56) into Eq. (54), we find that

$$S_{I,pl}(\omega) = \frac{6.95 \sigma_R^2}{\omega_t} \text{Re} \left\{ \left(\frac{\omega}{\omega_t} \right)^{-8/3} \left[1 - {}_1F_1 \left(-\frac{5}{6}; -\frac{1}{3}; -\frac{i\omega^2}{2\omega_t^2} \right) \right] \right. \\ \left. - 0.72 i^{4/3} {}_1F_1 \left(\frac{1}{2}; \frac{7}{3}; -\frac{i\omega^2}{2\omega_t^2} \right) \right\}. \quad (57)$$

where $\omega_t = V_\perp / \sqrt{L/k}$. The characteristic frequency ω_t , sometimes called the *Fresnel frequency*, is uniquely defined by the Fresnel scale and the mean wind speed.

The PSD (57), multiplied by ω_t and scaled by the scintillation index $\sigma_I^2(L) = \sigma_R^2$, is plotted in Fig. 8.13 (solid line). Observe that the PSD is essentially constant for $\omega < \omega_t$ and decays as $\omega^{-8/3}$ for $\omega > \omega_t$. Hence, the Fresnel frequency ω_t is the transition frequency at which the spectrum begins to decay.

8.5.2 Spherical wave

The transformation from spatial statistics to temporal statistics in the case of a spherical wave or beam wave is a little different because we have to account for the finite phase front radius of curvature, which is infinite (i.e., the phase front is planar) in the plane wave case. For example, we account for the phase front radius of curvature of the spherical wave by making the association $\xi \mathbf{p} \Rightarrow \mathbf{V}_\perp \tau$ in (49) or (52), from which we obtain the temporal covariance function. An exact analytic expression for the PSD associated with the irradiance

fluctuations of a spherical wave was derived by Clifford [21] using (49). However, from the approximation (52) we derive the simpler result

$$B_{I,\text{sp}}(\tau, L) = 8\pi^2 k^2 L \int_0^1 \int_0^\infty \kappa \Phi_n(\kappa) J_0(\kappa V_\perp \tau) \left\{ 1 - \cos \left[\frac{L\kappa^2}{k} \xi(1 - \xi) \right] \right\} d\kappa d\xi$$

$$\cong 3.87 \sigma_R^2 \text{Re} \left[0.40 i^{5/6} {}_1F_1 \left(-\frac{5}{6}; 1; \frac{9ikV_\perp^2 \tau^2}{8L} \right) - 0.47 \left(\frac{kV_\perp^2 \tau^2}{L} \right)^{5/6} \right], \quad (58)$$

which leads to

$$S_{I,\text{sp}}(\omega) = \frac{5.47 \sigma_R^2}{\omega_t} \text{Re} \left\{ \left(\frac{\omega}{\omega_t} \right)^{-8/3} \left[1 - {}_1F_1 \left(-\frac{5}{6}; -\frac{1}{3}; -\frac{2i\omega^2}{9\omega_t^2} \right) \right] \right. \\ \left. - 0.24 i^{4/3} {}_1F_1 \left(\frac{1}{2}; \frac{7}{3}; -\frac{2i\omega^2}{9\omega_t^2} \right) \right\}. \quad (59)$$

The PSD (59), scaled by $\sigma_{I,\text{sp}}^2(L) = 0.4\sigma_R^2$, is also plotted in Fig. 8.13 (dashed curve). Notice that the spherical wave spectrum (59) extends to somewhat higher frequencies than that of the plane wave.

8.5.3 Gaussian-beam wave

For the general case of a Gaussian-beam wave, the frozen turbulence hypothesis dictates that $\gamma \mathbf{p} \Rightarrow \mathbf{V}_\perp \boldsymbol{\tau}$ (and $\gamma^* \mathbf{p} \Rightarrow \mathbf{V}_\perp \boldsymbol{\tau}$), which accounts for the finite size of the Gaussian-beam wave as well as its phase front radius of curvature. The path amplitude parameter γ is defined by Eq. (20) in Chap. 6. Thus, based on Eq. (46), we make the association

$$J_0[\kappa|(1 - \bar{\Theta}\xi)\mathbf{p} - 2i\Lambda\xi\mathbf{r}|] = J_0\left(\kappa|\gamma\mathbf{p}/2 + \gamma^*\mathbf{p}/2 + \gamma\mathbf{r} - \gamma^*\mathbf{r}|\right) \quad (60)$$

$$\Rightarrow J_0(\kappa V_\perp \tau) I_0(2\Lambda\kappa\xi r),$$

where we have used the addition formula of the Bessel function² [(BJ8) in Appendix I]. Similarly, it follows that

$$J_0[(1 - \bar{\Theta}\xi - i\Lambda\xi)\kappa\rho] = J_0(\gamma\kappa\rho) \Rightarrow J_0(\kappa V_\perp \tau), \quad (61)$$

²Here we write (BJ8) as $\text{Re}[J_0(|\mathbf{Q}|)] = J_0(x)I_0(y) + 2\sum_{n=1}^{\infty}(-1)^n J_{2n}(x)I_{2n}(y)\cos 2n\phi$, where the vector $\mathbf{Q} = \mathbf{x} - i\mathbf{y}$ and ϕ is the angle between x and y [22]. Equation (60) is obtained by retaining only the first term on the right-hand side of this series.

and the resulting temporal covariance of the irradiance fluctuations is given by

$$B_I(\tau, \mathbf{r}, L) = 8\pi^2 k^2 L \int_0^1 \int_0^\infty \kappa \Phi_n(\kappa) \exp\left(-\frac{\Lambda L \xi^2 \kappa^2}{k}\right) J_0(\kappa V_\perp \tau) \\ \times \left\{ I_0(2\Lambda \kappa \xi r) - \cos\left[\frac{L \kappa^2}{k} \xi (1 - \bar{\Theta} \xi)\right] \right\} d\kappa d\xi. \quad (62)$$

If we use the above result for $r = 0$ and the phase screen analysis from Chap. 15, we are led to the (longitudinal) approximation

$$B_{I,l}(\tau, L) = 3.87 \sigma_R^2 \text{Re} \left\{ i^{5/6} [1 - (\bar{\Theta} + i\Lambda)d_t]^{5/6} {}_1F_1\left(-\frac{5}{6}; 1; -a_1 \omega_t^2 \tau^2\right) \right. \\ \left. - (\Lambda d_t)^{5/6} {}_1F_1\left(-\frac{5}{6}; 1; -a_2 \omega_t^2 \tau^2\right) \right\}, \quad (63)$$

where

$$a_1 = \frac{1}{4id_t[1 - (\bar{\Theta} + i\Lambda)d_t]}, \quad a_2 = \frac{1}{4\Lambda d_t^2}, \quad d_t = 0.67 - 0.17\bar{\Theta}. \quad (64)$$

The substitution of (63) into (54) yields the longitudinal power spectral density

$$S_{I,l}(\omega) = \frac{3.90 \sigma_R^2}{\omega_t d_t^{5/6}} \text{Re} \left\{ \left(\frac{\omega}{\omega_t}\right)^{-8/3} \left[{}_1F_1\left(-\frac{5}{6}; -\frac{1}{3}; -\frac{\omega^2}{4a_2 \omega_t^2}\right) \right. \right. \\ \left. \left. - {}_1F_1\left(-\frac{5}{6}; -\frac{1}{3}; -\frac{\omega^2}{4a_1 \omega_t^2}\right) + 0.29 t^{4/3} \right. \right. \\ \left. \left. \times \left[\frac{1}{a_2^{4/3}} {}_1F_1\left(\frac{1}{2}; \frac{7}{3}; -\frac{\omega^2}{4a_2 \omega_t^2}\right) - \frac{1}{a_1^{4/3}} {}_1F_1\left(\frac{1}{2}; \frac{7}{3}; -\frac{\omega^2}{4a_1 \omega_t^2}\right) \right] \right\}. \quad (65)$$

The PSD model (65) includes the plane wave and spherical wave results (57) and (59) as limiting cases. In Fig. 8.14 we plot the temporal power spectrum (65) for two collimated beams with Fresnel ratios $\Lambda_0 = 0.5$ and 5. Here we see that the general behavior is similar to that for the plane wave and spherical wave limiting cases illustrated in Fig. 8.13—namely, the Fresnel frequency $\omega_t = V_\perp / \sqrt{L/k}$ denotes that angular frequency at which the spectrum begins to fall off, where the mean transverse wind speed V_\perp plays an important role in determining spectral width.

In Fig. 8.15, we plot the quantity $\omega S_{I,l}(\omega) / 2\pi \sigma_I^2(0, L)$ deduced from (65) as a means of illustrating which scale sizes contribute most to power in the irradiance fluctuations. Here we show the same curves depicted in Fig. 8.14 and the other two curves are essentially the plane wave limit ($\Lambda_0 = 10^{-3}$) and spherical wave limit ($\Lambda_0 = 10^3$). The location of the peaks shows that the power in the spherical wave is concentrated in slightly smaller scales (higher frequency) than in the plane wave

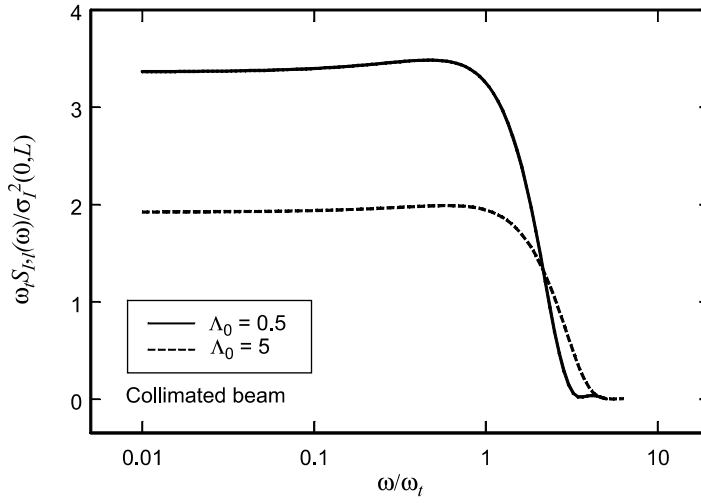


Figure 8.14 PSD of irradiance fluctuations of a collimated beam scaled by the on-axis scintillation index and multiplied by $\omega_t = V_\perp/\sqrt{L/k}$. Results are for $r = 0$ and the Kolmogorov power-law spectrum.

case. The peak values in the beam wave cases generally lie somewhere between these two extremes.

To obtain the PSD at a point off the optical axis, we must also include a radial term of the temporal covariance function, viz.,

$$B_{I,r}(\tau, \mathbf{r}, L) = 6.45 \sigma_R^2 (\Lambda d_t)^{5/6} \left(\frac{r^2}{W^2} \right) {}_1F_1 \left(\frac{1}{6}; 1; -\frac{\omega_t^2 \tau^2}{4\Lambda d_t^2} \right), \quad (66)$$

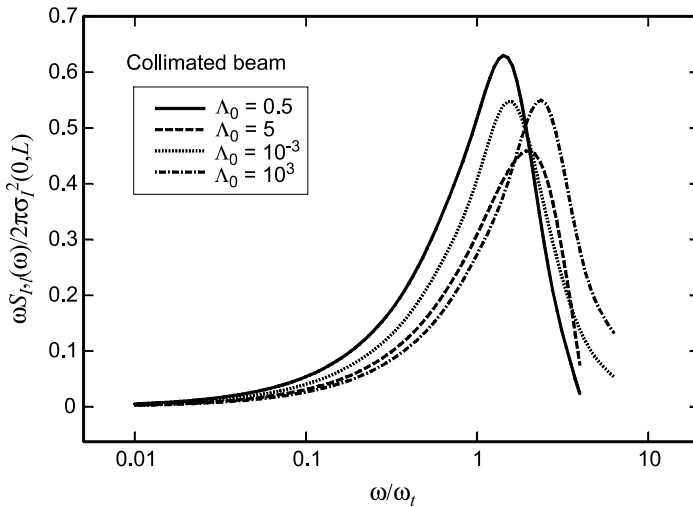


Figure 8.15 Scaled PSD of various size beam waves. Results are for $r = 0$ and based on the Kolmogorov spectrum.

which is deduced from Eq. (62). The substitution of this expression into (54) produces a radially dependent term for the spectrum [in addition to (65)] given by

$$S_{I,r}(\omega, r) = \frac{6.14 \sigma_R^2 \Lambda d_t^{7/6}}{\omega_t} \left(\frac{r^2}{W^2} \right) \left(\frac{\omega}{\omega_t} \right)^{-2/3} \left[{}_1F_1 \left(\frac{1}{6}; \frac{2}{3}; -\frac{\Lambda d_t^2 \omega^2}{\omega_t^2} \right) - 0.965 (\Lambda d_t^2)^{1/6} \left(\frac{\omega}{\omega_t} \right)^{1/3} {}_1F_1 \left(\frac{1}{2}; \frac{4}{3}; -\frac{\Lambda d_t^2 \omega^2}{\omega_t^2} \right) \right]. \quad (67)$$

The total PSD model is then the sum of (65) and (67), i.e.,

$$S_I(\omega, r) = S_{I,l}(\omega) + S_{I,r}(\omega, r). \quad (68)$$

In Fig. 8.16 we plot the PSD (68) scaled by the Rytov variance for $\Lambda_0 = 0.5$ and radial positions $r/W = 0, 0.1, 0.5$. Here we see that inclusion of the radial term causes the low-frequency range to increase over that on the optical axis, i.e., off-axis fluctuations are stronger than on-axis fluctuations and, moreover, are caused by the larger scales. These results are consistent with those given in Fig. 8 of Shelton [23] for a slant path to a geostationary satellite.

We plot the scaled PSD $\omega S_I(\omega, r)/\sigma_R^2$ deduced from (59) in Fig. 8.17, corresponding to the same beam illustrated in Fig. 8.16. In this case we note that the peak values of the PSD are all roughly the same as we move further away from the optical axis. However, the PSD once again tends to be higher at lower frequencies for larger values of r/W .

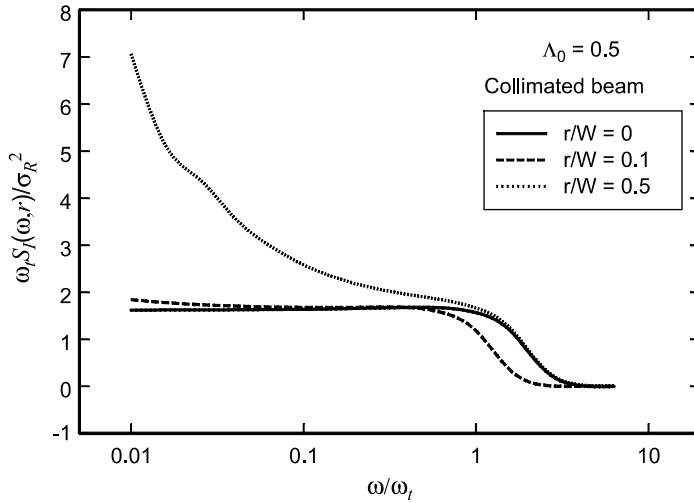


Figure 8.16 PSD for irradiance fluctuations illustrating the dependence upon radial position in the beam. Here, W is the beam radius in free space at the receiver.

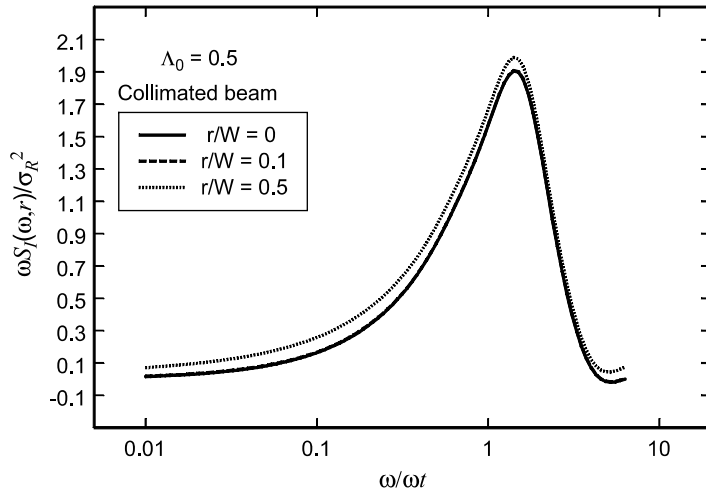


Figure 8.17 Scaled PSD for various radial positions off the optical axis. Results are based on the Kolmogorov spectrum.

8.6 Phase Fluctuations

In general, many of the same considerations arise in studying phase fluctuations as those that arise in studying irradiance fluctuations. However, there are important differences. In particular, the important scale sizes in irradiance fluctuations are small scales on the order of the Fresnel zone $\sqrt{L/k}$ or inner scale l_0 , whereas it is the larger scale sizes (including the outer scale) that affect phase fluctuations. As a result, a geometrical optics approximation is often used in studying the latter rather than full diffraction theory. Because the small wave number regime of the refractive-index power spectrum is not well defined for scale sizes on the order of the outer scale L_0 and larger, many early investigations centered on the phase structure function rather than on the covariance function.

The complex phase perturbation $\psi(\mathbf{r}, L)$ can be expressed as the sum

$$\psi(\mathbf{r}, L) = \chi(\mathbf{r}, L) + iS(\mathbf{r}, L), \quad (69)$$

where $\chi(\mathbf{r}, L)$ is called the *log amplitude* (see Section 8.2) and $S(\mathbf{r}, L)$ is the *phase*. Thus, we can express the phase in the form

$$S(\mathbf{r}, L) = \frac{1}{2i} [\psi(\mathbf{r}, L) - \psi^*(\mathbf{r}, L)], \quad (70)$$

where in general we assume $\psi(\mathbf{r}, L)$ contains both first-order and second-order perturbations, which yields

$$\begin{aligned} \psi(\mathbf{r}, L) &= \psi_1(\mathbf{r}, L) + \psi_2(\mathbf{r}, L) \\ &= \chi_1(\mathbf{r}, L) + \chi_2(\mathbf{r}, L) + i[S_1(\mathbf{r}, L) + S_2(\mathbf{r}, L)]. \end{aligned} \quad (71)$$

For the first-order perturbation $\psi_1(\mathbf{r}, L) = \chi_1(\mathbf{r}, L) + S_1(\mathbf{r}, L)$, the mean value is zero, and hence, $\langle \chi_1(\mathbf{r}, L) \rangle = \langle S_1(\mathbf{r}, L) \rangle = 0$. This is not the case, however, for the second-order terms (see Example 3 in Section 8.9).

8.6.1 Phase variance

Using Eq. (70), we find that (like the log-amplitude variance) the variance of the phase fluctuations of a Gaussian-beam wave propagating through homogeneous and isotropic turbulence depends only on the first-order complex phase perturbation $\psi_1(\mathbf{r}, L)$. Also, because $\langle S_1(\mathbf{r}, L) \rangle = 0$, the phase variance leads to

$$\begin{aligned}\sigma_s^2(\mathbf{r}, L) &= \langle S_1^2(\mathbf{r}, L) \rangle \\ &= \frac{1}{2} \text{Re}[\langle \psi_1(\mathbf{r}, L) \psi_1^*(\mathbf{r}, L) \rangle - \langle \psi_1(\mathbf{r}, L) \psi_1(\mathbf{r}, L) \rangle] \\ &= \frac{1}{2} \text{Re}[E_2(\mathbf{r}, \mathbf{r}) - E_3(\mathbf{r}, \mathbf{r})].\end{aligned}\quad (72)$$

Consequently, based on (3) and (4), we deduce that

$$\begin{aligned}\sigma_s^2(\mathbf{r}, L) &= 2\pi^2 k^2 L \int_0^1 \int_0^\infty \kappa \Phi_n(\kappa) \exp\left(-\frac{\Lambda L \kappa^2 \xi^2}{k}\right) \\ &\quad \times \left\{ I_0(2\Lambda r \kappa \xi) + \cos\left[\frac{L \kappa^2}{k} \xi(1 - \bar{\Theta} \xi)\right] \right\} d\kappa d\xi,\end{aligned}\quad (73)$$

which differs from the variance of log amplitude (12) only by the change in sign between the last two terms.

For the limiting case of a plane wave ($\Theta = 1$, $\Lambda = 0$) the phase variance (73) reduces to

$$\begin{aligned}\sigma_{s, \text{pl}}^2(L) &= 2\pi^2 k^2 L \int_0^1 \int_0^\infty \kappa \Phi_n(\kappa) \left[1 + \cos\left(\frac{L \kappa^2 \xi}{k}\right) \right] d\kappa d\xi \\ &\cong 4\pi^2 k^2 L \int_0^\infty \kappa \Phi_n(\kappa) d\kappa,\end{aligned}\quad (74)$$

where the last step is the result of a *geometrical optics approximation* ($L \kappa^2/k \ll 1$). We recognize this last integral as equivalent to a multiple of $E_1(0, 0)$ defined by Eq. (21) in Chap. 6. Hence, based on the von Kármán spectrum (25) it follows that the phase variance under a geometrical optics approximation can be written as

$$\sigma_{s, \text{pl}}^2(L) = 0.78 C_n^2 k^2 L \kappa_0^{-5/3}. \quad (75)$$

Phase measurements [24] have confirmed this last expression. Although Eq. (75) is based on a point receiver, it has been shown that phase noise cannot be suppressed by the use of a large-aperture receiver (unlike that of scintillation as discussed in

Chap. 10). (See Wheelon [19,25] for a discussion of aperture smoothing and general phase fluctuations, along with references to many early measurements.)

To include diffraction effects in the phase variance we need to retain the cosine term in (74). By recalling the definition of the log-amplitude variance given by (12), we note that

$$\sigma_{\chi, \text{pl}}^2(L) + \sigma_{S, \text{pl}}^2(L) = 4\pi^2 k^2 L \int_0^\infty \kappa \Phi_n(\kappa) d\kappa, \quad (76)$$

and from $\sigma_{\chi, \text{pl}}^2(L) = \sigma_{I, \text{pl}}^2(L)/4 = 0.31 C_n^2 k^{7/6} L^{11/6}$ and Eq. (75) above, we can write the phase variance for a plane wave given in (76) in the form

$$\begin{aligned} \sigma_{S, \text{pl}}^2(L) &= 0.78 C_n^2 k^2 L \kappa_0^{-5/3} - 0.31 C_n^2 k^{7/6} L^{11/6} \\ &= 0.64 \sigma_R^2 Q_0^{-5/6} \left(1 - 0.39 Q_0^{5/6}\right), \end{aligned} \quad (77)$$

where $Q_0 = L\kappa_0^2/k$. Clearly, the second term in (77) due to diffraction adds only a small correction to the geometrical optics expression (75).

For the case of a Gaussian-beam wave, the expression for the phase variance is somewhat different. First, we recognize that

$$\begin{aligned} \sigma_\chi^2(\mathbf{r}, L) + \sigma_S^2(\mathbf{r}, L) &= 4\pi^2 k^2 L \int_0^1 \int_0^\infty \kappa \Phi_n(\kappa) \\ &\quad \times \exp\left(-\frac{\Lambda L \kappa^2 \xi^2}{k}\right) I_0(2\Lambda r \kappa \xi) d\kappa d\xi, \end{aligned} \quad (78)$$

where, unlike the plane wave case, the phase variance for a Gaussian-beam wave depends on the radial position away from the optical axis. By rearranging terms in the integral on the right in (78), we can write the phase variance in terms of known quantities, i.e.,

$$\sigma_S^2(\mathbf{r}, L) = 4\pi^2 k^2 L \int_0^\infty \kappa \Phi_n(\kappa) d\kappa + 2\sigma_r^2(\mathbf{r}, L) - T - \sigma_\chi^2(\mathbf{r}, L), \quad (79)$$

where $\sigma_r^2(\mathbf{r}, L)$ and T are defined, respectively, by Eqs. (37) and (38) in Chap. 6. The variance of log amplitude $\sigma_\chi^2(\mathbf{r}, L)$ can be readily deduced from the scintillation index (13). By using the expressions (42) and (43) in Chap. 6, along with Eqs. (20) and (75) in the present chapter, we are led from (79) to the expression

$$\begin{aligned} \sigma_S^2(\mathbf{r}, L) &= 0.64 \sigma_R^2 Q_0^{-5/6} - 0.66 \sigma_R^2 \Lambda^{5/6} {}_1F_1\left(-\frac{5}{6}; 1; \frac{2r^2}{W^2}\right) \\ &\quad - 0.97 \sigma_R^2 \text{Re}\left[i^{5/6} {}_2F_1\left(-\frac{5}{6}, \frac{11}{6}; \frac{17}{6}; \bar{\Theta} + i\Lambda\right)\right]. \end{aligned} \quad (80)$$

In the limiting case of a plane wave, Eq. (80) reduces to (77) and for a spherical wave, we obtain

$$\sigma_{S, \text{sp}}^2(L) = 0.64 \sigma_R^2 Q_0^{-5/6} \left(1 - 0.16 Q_0^{5/6}\right). \quad (81)$$

Because the outer scale parameter $Q_0 \ll 1$ in most cases, we see that (80) is dominated by the lead term on the right, which is equivalent to the geometrical optics approximation (75) for the infinite plane wave. Thus, we generally expect to find little difference in the phase variance of a Gaussian-beam wave from that of a plane wave.

8.6.2 Phase structure function

In Section 6.4 we considered the wave structure function (WSF) which can be expressed in the form

$$D(\mathbf{r}_1, \mathbf{r}_2, L) = D_\chi(\mathbf{r}_1, \mathbf{r}_2, L) + D_S(\mathbf{r}_1, \mathbf{r}_2, L), \quad (82)$$

where $D_\chi(\mathbf{r}_1, \mathbf{r}_2, L)$ is the *log-amplitude structure function* and $D_S(\mathbf{r}_1, \mathbf{r}_2, L)$ is the *phase structure function*. These individual structure functions are defined, respectively, by

$$D_\chi(\mathbf{r}_1, \mathbf{r}_2, L) = \langle [\chi_1(\mathbf{r}_1, L) - \chi_1(\mathbf{r}_2, L)]^2 \rangle, \quad (83)$$

$$D_S(\mathbf{r}_1, \mathbf{r}_2, L) = \langle [S_1(\mathbf{r}_1, L) - S_1(\mathbf{r}_2, L)]^2 \rangle. \quad (84)$$

For the limiting case of a plane wave, these structure functions are defined explicitly by

$$D_{\chi,s}(\rho, L) = 4\pi^2 k^2 L \int_0^1 \int_0^\infty \kappa \Phi_n(\kappa) [1 - J_0(\kappa \rho)] \left[1 \mp \cos\left(\frac{L\kappa^2 \xi}{k}\right) \right] d\kappa d\xi, \quad (85)$$

where the upper sign corresponds to the log amplitude and the lower sign to the phase.

Under a geometrical optics approximation, the log-amplitude structure function is essentially zero and the phase structure function reduces to

$$D_{S,pl}(\rho, L) = 8\pi^2 k^2 L \int_0^\infty \kappa \Phi_n(\kappa) [1 - J_0(\kappa \rho)] d\kappa, \quad (86)$$

which is identical to the WSF for a plane wave (Section 6.4.1). Similarly, under the geometrical optics approximation the phase structure function of a spherical wave is

$$D_{S,sp}(\rho, L) = 8\pi^2 k^2 L \int_0^1 \int_0^\infty \kappa \Phi_n(\kappa) [1 - J_0(\kappa \xi \rho)] d\kappa d\xi. \quad (87)$$

The functional form of the structure functions (86) and (87) depends on the spatial separation between points on the phase front. For example, for small separation distances in which $\rho \ll l_0$, we can use the Tatarskii spectrum [Eq. (19) in Chap. 3] and the small-argument approximation for the Bessel function in (86) to obtain the plane wave result

$$\begin{aligned} D_{S,pl}(\rho, L) &= 2\pi^2 (0.033) C_n^2 k^2 L \rho^2 \int_0^\infty \kappa^{-2/3} \exp(-\kappa^2 / \kappa_m^2) d\kappa \\ &= 3.28 C_n^2 k^2 L l_0^{-1/3} \rho^2, \quad \rho \ll l_0. \end{aligned} \quad (88)$$

In the regime for which the separation distance satisfies $\rho \gg l_0$, we can use the von Kármán spectrum expressed in the form

$$\Phi_n(\kappa) = \frac{0.033 C_n^2}{(\kappa^2 + \kappa_0^2)^{11/6}}, \quad \kappa_0 \sim 1/L_0, \quad (89)$$

which is often used to characterize the small wave number regime (large scale sizes). However, the use of this spectrum model is based on the assumption that the eddies comparable in size with the outer scale and beyond are isotropic. In this case, we must evaluate

$$D_{S,pl}(\rho, L) = 2.606 C_n^2 k^2 L \int_0^\infty \frac{\kappa[1 - J_0(\kappa\rho)]}{(\kappa^2 + \kappa_0^2)^{11/6}} d\kappa, \quad (90)$$

which leads to

$$D_{S,pl}(\rho, L) = 1.56 C_n^2 k^2 L \kappa_0^{-5/3} [1 - (\kappa_0 \rho)^{5/6} K_{5/6}(\kappa_0 \rho)], \quad \rho \gg l_0. \quad (91)$$

For very large separation distances ($\rho \gg L_0$), the term involving the Bessel function in (91) tends to zero and we readily deduce that

$$D_{S,pl}(\rho, L) = 2\sigma_{S,pl}^2(L) = 1.56 C_n^2 k^2 L \kappa_0^{-5/3}, \quad \rho \gg L_0. \quad (92)$$

When the separation distance satisfies $l_0 \ll \rho \ll L_0$, the small-argument approximation of the Bessel function in (91) yields the inertial range form (see also Section 6.4)

$$D_{S,pl}(\rho, L) = 2.91 C_n^2 k^2 L \rho^{5/3}, \quad l_0 \ll \rho \ll L_0. \quad (93)$$

In Fig. 8.18 we plot the phase structure function (91) scaled by its large separation form (92). We also show the inertial range power-law behavior given by (93) for comparison. In this figure we see that the phase structure function departs from its inertial range form at relatively small separation distances.

To account for diffraction effects in the phase structure function, we again consider the plane wave case and write it in the form

$$\begin{aligned} D_{S,pl}(\rho, L) &= 4\pi^2 k^2 L \int_0^1 \int_0^\infty \kappa \Phi_n(\kappa) [1 - J_0(\kappa\rho)] \left[1 + \cos\left(\frac{L\kappa^2\xi}{k}\right) \right] d\kappa d\xi \\ &= \frac{1}{2} D_{pl}(\rho, L) + 4\pi^2 k^2 L \int_0^1 \int_0^\infty \kappa \Phi_n(\kappa) [1 - J_0(\kappa\rho)] \cos\left(\frac{L\kappa^2\xi}{k}\right) d\kappa d\xi. \end{aligned} \quad (94)$$

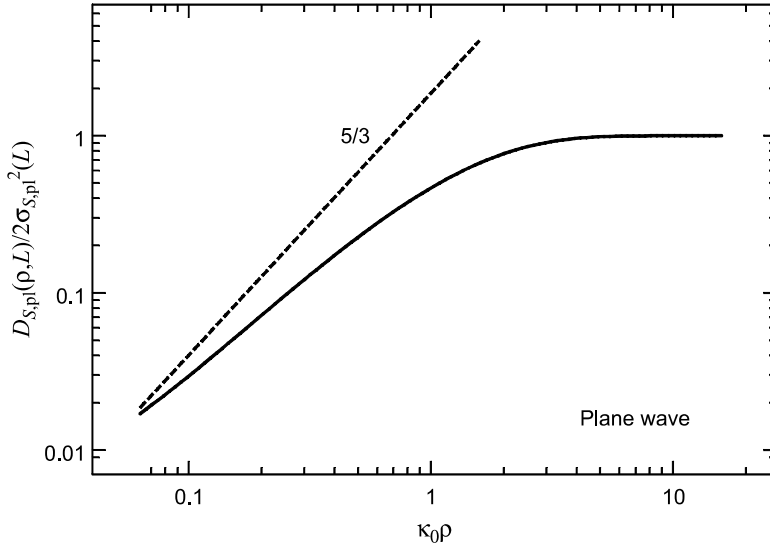


Figure 8.18 Phase structure function for a plane wave scaled by twice the phase variance as a function of scaled separation distance. The 5/3 inertial range power-law behavior is also shown (dashed line).

Upon evaluation of the double integral in (94), we get

$$D_{S,pl}(\rho, L) = \frac{1}{2} D_{pl}(\rho, L) + 1.94 \sigma_R^2 \text{Re} \left\{ i^{5/6} \left[{}_1F_1 \left(-\frac{5}{6}; 1; \frac{ik\rho^2}{2L} \right) - 1 \right] \right\}, \quad l_0 \ll \rho \ll L_0. \quad (95)$$

In arriving at this last expression, we have used the same approximation that led to (51). For $l_0 \ll \rho \ll \sqrt{L/k}$, it is easy to show (using the small-argument approximation for the confluent hypergeometric function) that (95) reduces to

$$D_{S,pl}(\rho, L) = \frac{1}{2} D_{pl}(\rho, L) = 1.46 C_n^2 k^2 L \rho^{5/3}, \quad l_0 \ll \rho \ll \sqrt{L/k}. \quad (96)$$

Note that (96) is only $\frac{1}{2}$ of the geometrical optics approximation (93) for separation distances smaller than the scale size of the first Fresnel zone $\sqrt{L/k}$. For larger separation distances satisfying $\sqrt{L/k} \ll \rho \ll L_0$, we can use the large-argument approximation for the confluent hypergeometric function to obtain

$$D_{S,pl}(\rho, L) = D_{pl}(\rho, L) = 2.91 C_n^2 k^2 L \rho^{5/3}, \quad \sqrt{L/k} \ll \rho \ll L_0. \quad (97)$$

Thus, for separation distances greater than the Fresnel scale we have the same expression given by (93) based on geometrical optics.

For the general Gaussian-beam wave, we restrict the analysis to the case $\mathbf{r}_2 = -\mathbf{r}_1$, which leads to the expression (including diffraction effects)

$$D_S(\rho, L) = 8\pi^2 k^2 L \int_0^1 \int_0^\infty \kappa \Phi_n(\kappa) \exp\left(-\frac{\Lambda L \kappa^2 \xi^2}{k}\right) \times \{I_0(\Lambda \rho \kappa \xi) - J_0[(1 - \bar{\Theta}\xi)\kappa\rho]\} d\kappa d\xi + 2[B_\chi(\rho, L) - B_\chi(0, L)]. \quad (98)$$

The integral on the right in (98) is recognized as the WSF [Eq. (73) in Chap. 6]. Based on Eq. (74) in Chap. 6 and the approximation for the covariance function given by (50) in the present chapter, we arrive at the phase structure function

$$D_S(\rho, L) = 0.89 \sigma_R^2 \left[a \left(\frac{k\rho^2}{L} \right)^{5/6} + 0.62 \Lambda^{11/6} \left(\frac{k\rho^2}{L} \right) \right] + 1.94 \sigma_R^2 \operatorname{Re} \left\{ (\Lambda d_t)^{5/6} - i^{5/6} [1 - (\bar{\Theta} + i\Lambda)d_t]^{5/6} + i^{5/6} [1 - (\bar{\Theta} + i\Lambda)d_t]^{5/6} {}_1F_1 \left[-\frac{5}{6}; 1; -\frac{(1 - \bar{\Theta}d_t - i\Lambda d_t)k\rho^2}{4i\Lambda d_t} \right] - (\Lambda d_t)^{5/6} {}_1F_1 \left[-\frac{5}{6}; 1; -\frac{k(1 - \bar{\Theta}d_t)^2 \rho^2}{4L\Lambda d_t^2} \right] \right\}, \quad l_0 \ll \rho \ll L_0, \quad (99)$$

where the parameter a is defined by Eq. (55) in Chap. 6. Under the geometrical optics approximation, the general result (99) reduces to the simpler expression

$$D_S(\rho, L) = 0.89 \sigma_R^2 \left[a \left(\frac{k\rho^2}{L} \right)^{5/6} + 0.62 \Lambda^{11/6} \left(\frac{k\rho^2}{L} \right) \right], \quad l_0 \ll \rho \ll L_0. \quad (100)$$

Except for small separation distances ($\rho \ll \sqrt{L/k}$), the phase structure function defined by (100) is much the same as that described by (99) based on diffraction theory.

8.6.3 Covariance function

Under the assumption that the turbulence is statistically homogeneous and isotropic, the structure function and covariance function of the phase are related by

$$D_S(\rho, L) = 2[B_S(0, L) - B_S(\rho, L)]. \quad (101)$$

Consequently, from Eq. (91) for the phase structure function of a plane wave, we can extract the *spatial covariance function*

$$B_{S,pl}(\rho, L) = 0.78 C_n^2 k^2 L \left(\frac{\rho}{\kappa_0} \right)^{5/6} K_{5/6}(\kappa_0 \rho), \quad \rho \gg l_0. \quad (102)$$

Like Eq. (91), the phase covariance function (102) is based on a geometrical optics approximation. To introduce diffraction effects into the covariance function, we start with the sum of covariance functions of phase and log amplitude for a plane wave

$$B_{S,pl}(\rho, L) + B_{\chi,pl}(\rho, L) = 2\pi^2 k^2 L \int_0^\infty \kappa \Phi_n(\kappa) J_0(\kappa \rho) d\kappa, \quad (103)$$

where the integral on the right-hand side is the geometrical optics approximation for the sum of covariance functions. Thus, relying on (102) and the covariance function of irradiance (51), we see that (103) leads to

$$\begin{aligned} B_{S,pl}(\rho, L) &= 0.64 \sigma_R^2 Q_0^{-5/6} (\kappa_0 \rho)^{5/6} K_{5/6}(\kappa_0 \rho) \\ &\quad - 0.97 \sigma_R^2 \text{Re} \left[i^{5/6} {}_1F_1 \left(-\frac{5}{6}; 1; \frac{ik\rho^2}{2L} \right) - 0.60 \left(\frac{k\rho^2}{L} \right)^{5/6} \right], \quad \rho \gg l_0. \end{aligned} \quad (104)$$

Once again, the first term on the right in (104) represents the dominant term, i.e., diffraction effects generally provide only a small correction.

The general case of a Gaussian-beam wave can be handled in a similar manner. First, we recognize that the sum of covariance functions in this case gives us

$$\begin{aligned} B_S(\mathbf{p}, \mathbf{r}, L) + B_\chi(\mathbf{p}, \mathbf{r}, L) &= 4\pi^2 k^2 L \text{Re} \int_0^1 \int_0^\infty \kappa \Phi_n(\kappa) \exp \left(-\frac{\Lambda L \kappa^2 \xi^2}{k} \right) \\ &\quad \times J_0[\kappa |(1 - \overline{\Theta}\xi)\mathbf{p} - 2i\Lambda\xi\mathbf{r}|] d\kappa d\xi \\ &= 4\pi^2 k^2 L \int_0^\infty \kappa \Phi_n(\kappa) J_0(\kappa \rho) d\kappa + \frac{1}{2} D_{pl}(\rho, L) \\ &\quad + \sigma_r^2(\mathbf{r}_1, L) + \sigma_r^2(\mathbf{r}_2, L) - T - \frac{1}{2} D(\mathbf{r}_1, \mathbf{r}_2, L), \end{aligned} \quad (105)$$

where we have rearranged terms in the double integral and $D(\mathbf{r}_1, \mathbf{r}_2, L)$ is defined by the real part of Eq. (39) in Chap. 6. To simplify this last result we set $\mathbf{r}_2 = -\mathbf{r}_1$, from which we deduce

$$\begin{aligned}
B_S(\rho, L) = & 0.64 \sigma_R^2 Q_0^{-5/6} (\kappa_0 \rho)^{5/6} K_{5/6}(\kappa_0 \rho) + 1.18 \sigma_R^2 \left(\frac{k \rho^2}{L} \right)^{5/6} - 1.33 \sigma_R^2 \Lambda^{5/6} \\
& \times {}_1F_1 \left(-\frac{5}{6}; 1; \frac{\rho^2}{2W^2} \right) - 0.44 \sigma_R^2 \left[a \left(\frac{k \rho^2}{L} \right)^{5/6} + 0.62 \Lambda^{11/6} \left(\frac{k \rho^2}{L} \right) \right] \\
& - 0.97 \sigma_R^2 \operatorname{Re} \left\{ i^{5/6} [1 - (\bar{\Theta} + i\Lambda) d_t]^{5/6} \right. \\
& \times {}_1F_1 \left[-\frac{5}{6}; 1; -\frac{(1 - \bar{\Theta} d_t - i\Lambda d_t) k \rho^2}{4i\Lambda d_t} \right] - (\Lambda d_t)^{5/6} \\
& \left. \times {}_1F_1 \left[-\frac{5}{6}; 1; -\frac{(1 - \bar{\Theta} d_t)^2 k \rho^2}{4L\Lambda d_t^2} \right] \right\}, \quad \rho \gg l_0, \tag{106}
\end{aligned}$$

where $d_t = 0.67 - 0.17\Theta$. In the limit of a plane wave ($\Theta = 1, \Lambda = 0$), Eq. (106) reduces to (104), whereas in the spherical wave limit ($\Theta = \Lambda = 0$) we obtain

$$\begin{aligned}
B_{S, \text{sp}}(\rho, L) = & 0.64 \sigma_R^2 Q_0^{-5/6} (\kappa_0 \rho)^{5/6} K_{5/6}(\kappa_0 \rho) + 0.74 \sigma_R^2 \left(\frac{k \rho^2}{L} \right)^{5/6} \\
& - 0.97 \sigma_R^2 \operatorname{Re} \left[0.40 i^{5/6} {}_1F_1 \left(-\frac{5}{6}; 1; \frac{ik \rho^2}{8L} \right) - 0.075 \left(\frac{k \rho^2}{L} \right)^{5/6} \right]. \tag{107}
\end{aligned}$$

8.6.4 Temporal power spectrum

By using the Taylor frozen-turbulence hypothesis, we can infer the temporal covariance function of a plane wave from the spatial covariance function by the replacement $\rho = \mathbf{V}_\perp \tau$, where \mathbf{V}_\perp is the mean wind velocity transverse to the propagation path. Consequently, the temporal covariance function is

$$B_{S, \text{pl}}(\tau, L) = 0.78 C_n^2 k^2 L \kappa_0^{-5/3} (\kappa_0 V_\perp \tau)^{5/6} K_{5/6}(\kappa_0 V_\perp \tau). \tag{108}$$

The power spectrum of phase fluctuations can now be defined similarly to that in Section 8.5 for the power spectrum of irradiance [see Eq. (54)]. Hence, by taking the Fourier transform of the temporal phase covariance function (108), we find that

$$\begin{aligned}
S_{S, \text{pl}}(\omega) = & 4 \int_0^\infty B_{S, \text{pl}}(\tau, L) \cos(\omega \tau) d\tau \\
= & 3.13 C_n^2 k^2 L \kappa_0^{-5/3} \int_0^\infty (\kappa_0 V_\perp \tau)^{5/6} K_{5/6}(\kappa_0 V_\perp \tau) \cos(\omega \tau) d\tau, \tag{109}
\end{aligned}$$

the evaluation of which yields [26]

$$S_{S,pl}(\omega) = \frac{5.82 C_n^2 k^2 L V_\perp^{5/3}}{(\omega^2 + \kappa_0^2 V_\perp^2)^{4/3}}. \quad (110)$$

Equation (110) represents the portion of the temporal phase spectrum of a plane wave due to large eddies. We now wish to also include the effects of diffraction and consider the more general Gaussian-beam wave case. Making use of the result of Eq. (60), we can convert the sum of spatial covariance functions given by (105) to the temporal expression

$$B_S(\tau, r, L) + B_\chi(\tau, r, L) = 4\pi^2 k^2 L \int_0^1 \int_0^\infty \kappa \Phi_n(\kappa) \\ \times J_0(\kappa V_\perp \tau) I_0(2\Lambda \kappa \xi r) d\kappa d\xi. \quad (111)$$

On the beam axis ($r = 0$), the evaluation of this integral combined with the result of (63) yields

$$B_S(\tau, 0, L) = 0.64 \sigma_R^2 Q_0^{-5/6} (\kappa_0 V_\perp \tau)^{5/6} K_{5/6}(\kappa_0 V_\perp \tau) \\ - 0.97 \sigma_R^2 \text{Re} \left\{ i^{5/6} [1 - (\bar{\Theta} + i\Lambda) d_t]^{5/6} {}_1F_1 \left(-\frac{5}{6}; 1; -a_1 \omega_t^2 \tau^2 \right) \right. \\ \left. - (\Lambda d_t)^{5/6} {}_1F_1 \left(-\frac{5}{6}; 1; -a_2 \omega_t^2 \tau^2 \right) \right\}. \quad (112)$$

The subsequent substitution of (112) into (54) provides us with an approximation for the longitudinal phase spectrum

$$S_S(\omega) = \frac{4.73 \sigma_R^2 \omega_t^{5/3}}{(\omega^2 + \kappa_0^2 V_\perp^2)^{4/3}} - \frac{0.97 \sigma_R^2}{\omega_t d_t^{5/6}} \text{Re} \left\{ \left(\frac{\omega}{\omega_t} \right)^{-8/3} \left[{}_1F_1 \left(-\frac{5}{6}; -\frac{1}{3}; -\frac{\omega^2}{4a_1 \omega_t^2} \right) \right. \right. \\ \left. \left. - {}_1F_1 \left(-\frac{5}{6}; -\frac{1}{3}; -\frac{\omega^2}{4a_1 \omega_t^2} \right) \right] + 0.29 i^{4/3} \left[\frac{1}{a_2^{4/3}} {}_1F_1 \left(\frac{1}{2}; \frac{7}{3}; -\frac{\omega^2}{4a_2 \omega_t^2} \right) \right. \right. \\ \left. \left. - \frac{1}{a_1^{4/3}} {}_1F_1 \left(\frac{1}{2}; \frac{7}{3}; -\frac{\omega^2}{4a_1 \omega_t^2} \right) \right] \right\}. \quad (113)$$

By multiplying this expression by ω and regrouping terms, we arrive at

$$\begin{aligned} \omega S_S(\omega) = & \frac{4.73 \sigma_R^2 Q_0^{-5/6} (\omega/\kappa_0 V_\perp)}{(\omega^2/\kappa_0^2 V_\perp^2 + 1)^{4/3}} - \frac{0.97 \sigma_R^2 Q_0^{1/2} (\omega/\kappa_0 V_\perp)}{d_t^{5/6}} \\ & \times \operatorname{Re} \left\{ Q_0^{-4/3} \left(\frac{\omega}{\kappa_0 V_\perp} \right)^{-8/3} \left[{}_1F_1 \left(-\frac{5}{6}; -\frac{1}{3}; -\frac{Q_0 \omega^2}{4a_2 \kappa_0^2 V_\perp^2} \right) \right. \right. \\ & \left. \left. - {}_1F_1 \left(-\frac{5}{6}; -\frac{1}{3}; -\frac{Q_0 \omega^2}{4a_1 \kappa_0^2 V_\perp^2} \right) \right] + 0.29 i^{4/3} \right. \\ & \left. \times \left[\frac{1}{a_2^{4/3}} {}_1F_1 \left(\frac{1}{2}; \frac{7}{3}; -\frac{Q_0 \omega^2}{4a_2 \kappa_0^2 V_\perp^2} \right) - \frac{1}{a_1^{4/3}} {}_1F_1 \left(\frac{1}{2}; \frac{7}{3}; -\frac{Q_0 \omega^2}{4a_1 \kappa_0^2 V_\perp^2} \right) \right] \right\}. \end{aligned} \quad (114)$$

In Fig. 8.19 we plot (114), scaled by the on-axis ($r = 0$) phase variance (80), as a function of $\omega/\kappa_0 V_\perp$ for three different collimated Gaussian-beam waves with $Q_0 = 10^{-3}$. The beam corresponding to $\Lambda_0 = 10^{-3}$ is similar to that of a plane wave and the beam corresponding to $\Lambda_0 = 10^3$ is similar to that of a spherical wave. This behavior is consistent with that displayed by the experimental data obtained by Lukin and Pokasov [27]. Note that there is no significant difference in the three beams for frequencies $\omega < 20\kappa_0 V_\perp$. Consequently, except for frequencies $\omega \gg 20\kappa_0 V_\perp$, the spectrum can be closely approximated by the geometrical optics expression given by the first term on the right in Eq. (113).

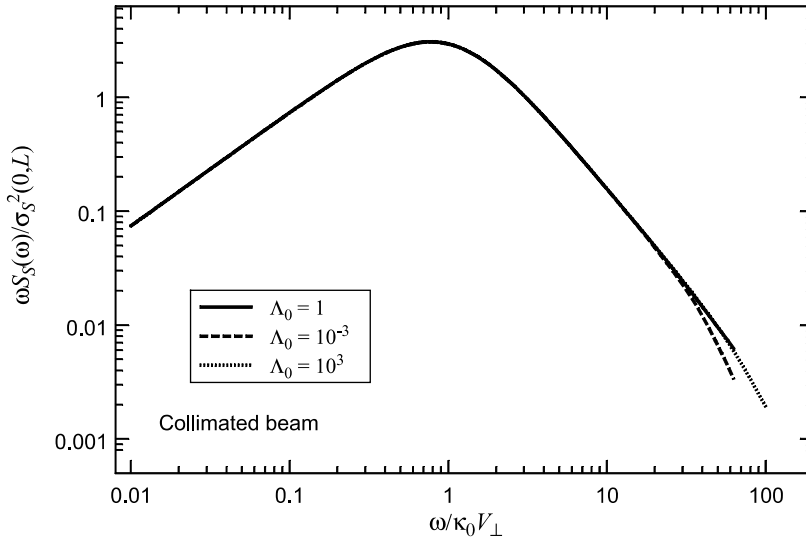


Figure 8.19 Normalized phase spectrum multiplied by ω and plotted as a function of $\omega/\kappa_0 V_\perp$. The outer scale is chosen so that the non-dimensional parameter $Q_0 = L\kappa_0^2/k = 10^{-3}$.

8.7 Slant Paths

The general expressions developed above for irradiance fluctuations and phase fluctuations no longer apply when the refractive-index structure parameter C_n^2 changes along the propagation path. To account for such changes, we will follow the approach introduced in Section 6.8. Further discussion of these statistical quantities for propagation paths from ground/aircraft to space or from space to ground/aircraft will be taken up in Chap. 12.

8.7.1 Irradiance fluctuations

The scintillation index for a Gaussian-beam wave is defined by the integral in Eq. (14). For varying index-of-refraction structure parameter and the special case of an infinite *plane wave*, we find that (14) reduces to

$$\begin{aligned}\sigma_{I,pl}^2(L) &= 8\pi^2 k^2 \int_0^L \int_0^\infty \kappa \Phi_n(\kappa, z) \left[1 - \cos \frac{L\kappa^2(1-z/L)}{k} \right] d\kappa dz \\ &= 2.25 k^{7/6} L^{5/6} \int_0^L C_n^2(z) (1-z/L)^{5/6} dz.\end{aligned}\quad (115)$$

Note that the integral in (115) weighs values of the structure parameter $C_n^2(z)$ near the transmitter more heavily than those near the receiver. Similarly, for a *spherical wave* we are led to

$$\begin{aligned}\sigma_{I,sp}^2(L) &= 8\pi^2 k^2 \int_0^L \int_0^\infty \kappa \Phi_n(\kappa, z) \left[1 - \cos \frac{\kappa^2 z(1-z/L)}{k} \right] d\kappa dz \\ &= 2.25 k^{7/6} \int_0^L C_n^2(z) z^{5/6} (1-z/L)^{5/6} dz,\end{aligned}\quad (116)$$

whereas in the general *Gaussian-beam wave* case, we obtain

$$\sigma_I^2(\mathbf{r}, L) = \sigma_{I,r}^2(\mathbf{r}, L) + \sigma_{I,l}^2(L). \quad (117)$$

For the *untracked beam*, the total scintillation index (117) is

$$\begin{aligned}\sigma_I^2(\mathbf{r}, L)_{\text{untracked}} &= 14.50 k^{7/6} L^{5/6} \Lambda^{5/6} \left(\frac{r - \sigma_{pe}}{W} \right)^2 \int_0^L C_n^2(z) (1-z/L)^{5/3} dz \\ &\quad + 14.50 k^{7/6} L^{5/6} \Lambda^{5/6} \left(\frac{\sigma_{pe}}{W} \right)^2 \int_0^L C_n^2(z) (1-z/L)^{5/3} dz \\ &\quad + 8.70 k^{7/6} L^{5/6} \text{Re} \int_0^L C_n^2(z) \left\{ i^{5/6} (1-z/L)^{5/6} \right. \\ &\quad \times [1 - (\bar{\Theta} + i\Lambda)(1-z/L)]^{5/6} \\ &\quad \left. - \Lambda^{5/6} (1-z/L)^{5/3} \right\} dz, \quad \sigma_{pe} \leq r < W,\end{aligned}\quad (118)$$

where the first term on the right represents the off-axis contribution in the radial direction and the remaining terms correspond to the longitudinal component. In the case of a *tracked beam*, the corresponding expression becomes

$$\begin{aligned}\sigma_I^2(\mathbf{r}, L)_{\text{tracked}} = & 14.50 k^{7/6} L^{5/6} \Lambda^{5/6} \left(\frac{r - \sqrt{\langle r_c^2 \rangle}}{W} \right)^2 \int_0^L C_n^2(z) (1 - z/L)^{5/3} dz \\ & + 8.70 k^{7/6} L^{5/6} \text{Re} \int_0^L C_n^2(z) \left\{ i^{5/6} (1 - z/L)^{5/6} \right. \\ & \times [1 - (\bar{\Theta} + i\Lambda)(1 - z/L)]^{5/6} - \Lambda^{5/6} (1 - z/L)^{5/3} \left. \right\} dz, \\ & \sqrt{\langle r_c^2 \rangle} \leq r < W. \quad (119)\end{aligned}$$

In (118) and (119), the rms beam wander displacement and rms pointing error displacement can be deduced from (33) and (36), respectively, by including the refractive-index structure parameter under the integral (see also Chap. 12).

All of the above results are based on the Kolmogorov spectrum

$$\Phi_n(\kappa, z) = 0.033 C_n^2(z) \kappa^{-11/3}. \quad (120)$$

In principle, similar results can be developed for more general spectral models like the modified atmospheric spectrum featuring inner scale and outer scale parameters. However, when the structure parameter varies along the path it is reasonable to assume that inner scale and outer scale values also change as a function of propagation distance z and, unfortunately, such relations are still generally unknown.

Again using the spectral model (120), the corresponding covariance function of the irradiance fluctuations is given by

$$\begin{aligned}B_I(\rho, L) = & 8.70 k^{7/6} L^{5/6} \text{Re} \int_0^L C_n^2(z) \left\{ i^{5/6} \xi^{5/6} [1 - (\bar{\Theta} + i\Lambda)\xi]^{5/6} \right. \\ & \times {}_1F_1 \left[-\frac{5}{6}; 1; -\frac{k\rho^2[1 - (\bar{\Theta} + i\Lambda)\xi]}{4iL\xi} \right] \\ & \left. - \Lambda^{5/6} \xi^{5/3} {}_1F_1 \left[-\frac{5}{6}; 1; -\frac{k\rho^2}{4L\Lambda} \left(\frac{1 - \bar{\Theta}\xi}{\xi} \right)^2 \right] \right\} dz,\end{aligned} \quad (121)$$

where $\rho = |\mathbf{r} - (-\mathbf{r})| = 2r$ is the distance between two points symmetrically located with respect to the optical axis and $\xi = 1 - z/L$. Clearly, Eq. (121) reduces to the longitudinal component of the scintillation index (119) for $\rho = 0$.

For an infinite plane wave, we find that (121) reduces to

$$B_{I,pl}(\rho, L) = 8.70 k^{7/6} L^{5/6} \operatorname{Re} \int_0^L C_n^2(z) \left\{ i^{5/6} \left(1 - \frac{z}{L}\right)^{5/6} \times {}_1F_1 \left[-\frac{5}{6}; 1; -\frac{k\rho^2}{4iL(1-z/L)} \right] - 1.06 \left(\frac{k\rho^2}{4L} \right)^{5/6} \right\} dz, \quad (122)$$

whereas for a spherical wave,

$$B_{I,sp}(\rho, L) = 8.70 k^{7/6} L^{5/6} \operatorname{Re} \int_0^L C_n^2(z) \left\{ i^{5/6} \left(\frac{z}{L} \right)^{5/6} \left(1 - \frac{z}{L}\right)^{5/6} \times {}_1F_1 \left[-\frac{5}{6}; 1; -\frac{k\rho^2 z/L}{4iL(1-z/L)} \right] - 1.06 \left(\frac{k\rho^2}{4L} \right)^{5/6} \left(\frac{z}{L} \right)^{5/3} \right\} dz. \quad (123)$$

8.7.2 Phase fluctuations

For constant C_n^2 along the propagation path, the phase variance is defined by (75). If we now assume that C_n^2 varies along the path, then we write

$$\begin{aligned} \sigma_{S,pl}^2(L) &\cong 4\pi^2 k^2 \int_0^L \int_0^\infty \kappa \Phi_n(\kappa, z) d\kappa dz \\ &= 0.78 k^2 \kappa_0^{-5/3} \int_0^L C_n^2(z) dz, \end{aligned} \quad (124)$$

where we are tacitly assuming that the outer scale $L_0 = 2\pi/\kappa_0$ can be approximated by some average value in accordance with the von Kármán spectrum

$$\Phi_n(\kappa, z) = \frac{0.033 C_n^2(z)}{(\kappa^2 + \kappa_0^2)^{11/6}}. \quad (125)$$

Although derived for an infinite plane wave, Eq. (124) generally holds for the more general Gaussian-beam wave under a variety of conditions. Similarly, the phase structure function for an infinite plane wave can be deduced from (90), which for the spectrum (125) leads to

$$D_{S,pl}(\rho, L) = 1.56 k^2 \kappa_0^{-5/3} [1 - (\kappa_0 \rho)^{5/6} K_{5/6}(\kappa_0 \rho)] \int_0^L C_n^2(z) dz, \quad \rho \gg l_0, \quad (126)$$

and the related covariance function becomes

$$B_{S,pl}(\rho, L) = 0.78 k^2 \left(\frac{\rho}{\kappa_0} \right)^{5/6} K_{5/6}(\kappa_0 \rho) \int_0^L C_n^2(z) dz, \quad \rho \gg l_0. \quad (127)$$

8.8 Summary and Discussion

The general *fourth-order moment* of the field is a cross-coherence function between four spatial points in the receiver plane. Its general form is too complex to be very useful, but specializations of it involving only one or two points in the receiver plane lead to the *scintillation index* and the *covariance function* of the irradiance.

The *scintillation index* is the *normalized irradiance variance* of the optical wave defined by

$$\sigma_I^2 = \frac{\langle I^2 \rangle}{\langle I \rangle^2} - 1. \quad (128)$$

Under the assumption of weak fluctuation theory, the scintillation index is related to the log-amplitude variance σ_χ^2 according to $\sigma_I^2 = \exp(4\sigma_\chi^2) - 1 \cong 4\sigma_\chi^2$. Consequently, using the Kolmogorov spectrum and standard Rytov theory, the defining integral for the scintillation index leads to (neglecting beam wander considerations)

$$\begin{aligned} \sigma_I^2(\mathbf{r}, L) = 2.65 \sigma_R^2 \Lambda^{5/6} & \left[1 - {}_1F_1\left(-\frac{5}{6}; 1; \frac{2r^2}{W^2}\right) \right] \\ & + 3.86 \sigma_R^2 \operatorname{Re} \left[i^{5/6} {}_2F_1\left(-\frac{5}{6}, \frac{11}{6}; \frac{17}{6}; \overline{\Theta} + i\Lambda\right) - \frac{11}{16} \Lambda^{5/6} \right]. \end{aligned} \quad (129)$$

In many cases, however, it is sufficient to approximate (129) by

$$\begin{aligned} \sigma_I^2(\mathbf{r}, L) = 4.42 \sigma_R^2 \Lambda^{5/6} \frac{r^2}{W^2} + 3.86 \sigma_R^2 & \left\{ 0.40[(1 + 2\overline{\Theta})^2 + 4\Lambda^2]^{5/12} \right. \\ & \times \cos\left[\frac{5}{6} \tan^{-1}\left(\frac{1 + 2\overline{\Theta}}{2\Lambda}\right)\right] - \frac{11}{16} \Lambda^{5/6} \Big\}, \quad r < W. \end{aligned} \quad (130)$$

This last expression is an accurate approximation to (129) except for large-aperture focused beams. These expressions show that, under weak irradiance fluctuations, the scintillation index varies linearly with the refractive-index structure parameter C_n^2 (or the Rytov variance σ_R^2). This is not the case for strong fluctuations (Chap. 9).

Scintillations are caused primarily by small-scale inhomogeneities roughly on the order of the Fresnel zone scale $\sqrt{L/k}$. Inner scale effects are negligible when the inner scale is much smaller than the size of the Fresnel zone. However, when the inner scale and Fresnel zone are of comparable size, the high-wave-number bump in the refractive-index spectrum [Eq. (22) in Chap. 3] causes the scintillations to increase over that predicted by the Kolmogorov spectrum [4–6]. But, weak irradiance scintillations are generally insensitive to

large-scale inhomogeneities of the medium, except near the beam edge. Outer scale effects tend to reduce scintillations for points off the beam axis, but have virtually no effect on unbounded plane waves, spherical waves, or along the optical axis of a Gaussian-beam wave. Scintillation of a Gaussian beam increases with the square of distance transverse to the optical axis and, thus, can lead to large values in the radial direction even though the scintillation level at the optical axis is well within the regime of weak fluctuation theory.

The behavior of irradiance fluctuations in the weak fluctuation regime for a finite beam is actually a combination of atmospherically induced scintillation and that caused by appreciable *beam wander*. For a collimated or divergent beam on a horizontal path, beam wander doesn't appear to have a strong effect on the irradiance fluctuations (e.g., see Fig. 8.9). For a convergent or focused beam, however, beam wander can have a significant impact, particularly near the optical axis of a larger beam (see Fig. 8.11). This causes us to redefine the longitudinal and radial components of scintillation, depending on whether the beam is tracked or not. For the *untracked beam* we have

$$\sigma_I^2(\mathbf{r}, L)_{\text{untracked}} = 4.42 \sigma_R^2 \Lambda^{5/6} \left(\frac{r - \sigma_{pe}}{W} \right)^2 + 4.42 \sigma_R^2 \Lambda^{5/6} \left(\frac{\sigma_{pe}}{W} \right)^2 + 3.86 \sigma_R^2$$

$$\times \text{Re} \left[i^{5/6} {}_2F_1 \left(-\frac{5}{6}, \frac{11}{6}; \frac{17}{6}; \bar{\Theta} + i\Lambda \right) - \frac{11}{16} \Lambda^{5/6} \right], \quad (131)$$

$$\sigma_{pe} \leq r < W.$$

where σ_{pe} is the rms pointing error [see (36)]. For the *tracked beam* case, we need to remove all beam wander effects from the radial term. However, other tracking methods will in general lead to different results. By removing the rms beam wander displacement from the radial component, using (33) for the beam wander variance, we find

$$\sigma_I^2(\mathbf{r}, L)_{\text{tracked}} = 4.42 \sigma_R^2 \Lambda^{5/6} \left(\frac{r - \sqrt{\langle r_c^2 \rangle}}{W} \right)^2 + 3.86 \sigma_R^2$$

$$\times \text{Re} \left[i^{5/6} {}_2F_1 \left(-\frac{5}{6}, \frac{11}{6}; \frac{17}{6}; \bar{\Theta} + i\Lambda \right) - \frac{11}{16} \Lambda^{5/6} \right], \quad (132)$$

$$\sqrt{\langle r_c^2 \rangle} \leq r < W.$$

As the strength of turbulence increases due to long path lengths and/or increasing values of C_n^2 , beam wander plays a lesser role and the beam begins to break up into a multitude of irregular-shaped spots, each acting somewhat like an independent beam.

All irradiance statistical quantities derived in this chapter are based on the notion of a “point receiver,” i.e., one in which its aperture size is much smaller than the lateral scale (*correlation width*) of the irradiance fluctuations (Section 8.4). The *irradiance covariance* of a Gaussian-beam wave based on two points on the phase front in which $\mathbf{r}_2 = -\mathbf{r}_1$ can be approximated by

$$B_I(\rho, L) = 3.87 \sigma_R^2 \text{Re} \left\{ i^{5/6} [1 - (\bar{\Theta} + i\Lambda) d_t]^{5/6} \right. \\ \times {}_1F_1 \left[-\frac{5}{6}; 1; -\frac{(1 - \bar{\Theta} d_t - i\Lambda d_t) k \rho^2}{4iL d_t} \right] \\ \left. - (\Lambda d_t)^{5/6} {}_1F_1 \left[-\frac{5}{6}; 1; -\frac{(1 - \bar{\Theta} d_t)^2 k \rho^2}{4L \Lambda d_t^2} \right] \right\}, \quad (133)$$

where $d_t = 0.67 - 0.17\bar{\Theta}$. In determining the correlation width ρ_c of the irradiance fluctuations, the Fresnel scale $\sqrt{L/k}$ emerges as the important parameter. For example, we find $\rho_c \sim 1.7\sqrt{L/k}$ for a plane wave, $\rho_c \sim 3\sqrt{L/k}$ for a spherical wave, and $\rho_c \sim \sqrt{L/k}$ for a collimated beam wave with Fresnel ratio $\Lambda_0 \sim 1$. For receiver apertures much larger than the Fresnel scale, aperture-averaging effects will lead to lower scintillation levels (Section 10.3). In the case of a slant path, the corresponding expression for a Gaussian-beam wave is ($\xi = 1 - z/L$)

$$B_I(\rho, L) = 8.70 k^{7/6} L^{5/6} \text{Re} \int_0^L C_n^2(z) \left\{ i^{5/6} \xi^{5/6} [1 - (\bar{\Theta} + i\Lambda) \xi]^{5/6} \right. \\ \times {}_1F_1 \left[-\frac{5}{6}; 1; -\frac{k \rho^2 [1 - (\bar{\Theta} + i\Lambda) \xi]}{4iL \xi} \right] \\ \left. - \Lambda^{5/6} \xi^{5/3} {}_1F_1 \left[-\frac{5}{6}; 1; -\frac{k \rho^2}{4L \Lambda} \left(\frac{1 - \bar{\Theta} \xi}{\xi} \right)^2 \right] \right\} dz, \quad (134)$$

The *temporal power spectrum* of irradiance fluctuations can be inferred by application of Taylor’s frozen-turbulence hypothesis. For a Gaussian-beam wave, this leads to the *temporal covariance function*

$$B_I(\tau, \mathbf{r}, L) = B_{I,l}(\tau, L) + B_{I,r}(\tau, \mathbf{r}, L), \quad (135)$$

where the longitudinal component is

$$B_{l,l}(\tau, L) = 3.87 \sigma_R^2 \text{Re} \left\{ i^{5/6} [1 - (\bar{\Theta} + i\Lambda)d_t]^{5/6} {}_1F_1\left(-\frac{5}{6}; 1; -a_1\omega_t^2\tau^2\right) \right. \\ \left. - (\Lambda d_t)^{5/6} {}_1F_1\left(-\frac{5}{6}; 1; -a_2\omega_t^2\tau^2\right) \right\}, \quad (136)$$

and where

$$a_1 = \frac{1}{4id_t[1 - (\bar{\Theta} + i\Lambda)d_t]}, \quad a_2 = \frac{1}{4\Lambda d_t^2}, \quad \omega_t = \frac{V_\perp}{\sqrt{L/K}}. \quad (137)$$

The corresponding radial component is

$$B_{l,r}(\tau, \mathbf{r}, L) = 6.45 \sigma_R^2 (\Lambda d_t)^{5/6} \left(\frac{r^2}{W^2} \right) {}_1F_1\left(\frac{1}{6}, 1, -\frac{\omega_t^2\tau^2}{4\Lambda d_t^2}\right). \quad (138)$$

The Fourier transform of (135) leads to the temporal power spectrum defined by

$$S_I(\omega, r) = S_{l,l}(\omega) + S_{l,r}(\omega, r), \quad (139)$$

where

$$S_{l,l}(\omega) = \frac{3.90 \sigma_R^2}{\omega_t d_t^{5/6}} \text{Re} \left\{ \left(\frac{\omega}{\omega_t} \right)^{-8/3} \left[{}_1F_1\left(-\frac{5}{6}; -\frac{1}{3}; -\frac{\omega^2}{4a_2\omega_t^2}\right) \right. \right. \\ \left. - {}_1F_1\left(-\frac{5}{6}; -\frac{1}{3}; -\frac{\omega^2}{4a_1\omega_t^2}\right) + 0.29i^{4/3} \left[\frac{1}{a_2^{4/3}} {}_1F_1\left(\frac{1}{2}; \frac{7}{3}; -\frac{\omega^2}{4a_2\omega_t^2}\right) \right. \right. \\ \left. \left. - \frac{1}{a_1^{4/3}} {}_1F_1\left(\frac{1}{2}; \frac{7}{3}; -\frac{\omega^2}{4a_1\omega_t^2}\right) \right] \right\}, \quad (140)$$

$$S_{l,r}(\omega, r) = \frac{6.14 \sigma_R^2 \Lambda d_t^{7/6}}{\omega_t} \left(\frac{r^2}{W^2} \right) \left(\frac{\omega}{\omega_t} \right)^{-2/3} \left[{}_1F_1\left(\frac{1}{6}; \frac{2}{3}; -\frac{\Lambda d_t^2 \omega^2}{\omega_t^2}\right) \right. \\ \left. - 0.97 (\Lambda d_t^2)^{1/6} \left(\frac{\omega}{\omega_t} \right)^{1/3} {}_1F_1\left(\frac{1}{2}; \frac{4}{3}; -\frac{\Lambda d_t^2 \omega^2}{\omega_t^2}\right) \right]. \quad (141)$$

The *Fresnel frequency* ω_t , which depends on the transverse wind velocity component V_\perp , represents the transition point at which the longitudinal component (140) of the power spectrum begins to decay as $\omega^{-8/3}$.

Whereas irradiance fluctuations are caused by scale sizes comparable with the Fresnel scale $\sqrt{L/k}$, phase fluctuations are caused primarily by scale sizes larger than the Fresnel scale. For this reason, phase fluctuations can generally be well approximated by the method of *geometrical optics*. That is, diffraction effects due to the smaller eddies usually provide only a small correction to the geometrical optics approximation.

For a Gaussian-beam wave, the *phase variance* generally depends on the radial position in the beam cross section and can be approximated by

$$\begin{aligned} \sigma_S^2(\mathbf{r}, L) = & 0.64 \sigma_R^2 Q_0^{-5/6} - 0.66 \sigma_R^2 \Lambda^{5/6} {}_1F_1\left(-\frac{5}{6}, 1; \frac{2r^2}{W^2}\right) \\ & - 0.97 \sigma_R^2 \text{Re}\left[i^{5/6} {}_2F_1\left(-\frac{5}{6}, \frac{11}{6}; \frac{17}{6}; \bar{\Theta} + i\Lambda\right)\right]. \end{aligned} \quad (142)$$

However, the lead term on the right in (142), which is the geometrical optics approximation, is the dominant factor in the phase variance. Along a slant path, the phase variance based on this lead term takes the form (assuming κ_0 is constant)

$$\sigma_S^2(\mathbf{r}, L) = 0.78 k^2 \kappa_0^{-5/3} \int_0^L C_n^2(z) dz. \quad (143)$$

The *phase structure function* provides a measure of the fluctuations associated with the difference of the phase at two points on the phase front. Under a geometrical optics approximation, the phase structure function is essentially the same as the wave structure function (WSF) studied in Chap. 6. Within the inertial range the phase structure function (including diffraction effects) can be approximated by

$$\begin{aligned} D_S(\rho, L) = & 0.89 \sigma_R^2 \left[a \left(\frac{k\rho^2}{L} \right)^{5/6} + 0.62 \Lambda^{11/6} \left(\frac{k\rho^2}{L} \right) \right] \\ & + 1.94 \sigma_R^2 \text{Re} \left\{ (\Lambda d_t)^{5/6} - i^{5/6} [1 - (\bar{\Theta} + i\Lambda) d_t]^{5/6} \right. \\ & + i^{5/6} [1 - (\bar{\Theta} + i\Lambda) d_t]^{5/6} {}_1F_1 \left[-\frac{5}{6}; 1; -\frac{(1 - \bar{\Theta} d_t - i\Lambda d_t) k\rho^2}{4iLd_t} \right] \\ & \left. - (\Lambda d_t)^{5/6} {}_1F_1 \left[-\frac{5}{6}; 1; -\frac{k(1 - \bar{\Theta} d_t)^2 \rho^2}{4L\Lambda d_t^2} \right] \right\}, \quad l_0 \ll \rho \ll L_0, \end{aligned} \quad (144)$$

where the parameter a is defined by

$$a = \begin{cases} \frac{1 - \Theta^{8/3}}{1 - \Theta}, & \Theta \geq 0 \\ \frac{1 + |\Theta|^{8/3}}{1 - \Theta}, & \Theta < 0. \end{cases} \quad (145)$$

The first term on the right in (144) represents the WSF, which is also the geometrical optics approximation to the phase structure function given by (100). Taking the outer scale into account and considering the limiting case of a plane wave along a slant path, it can be shown that

$$D_{S,pl}(\rho, L) = 1.56 k^2 \kappa_0^{-5/3} [1 - (\kappa_0 \rho)^{5/6} K_{5/6}(\kappa_0 \rho)] \times \int_0^L C_n^2(z) dz, \quad \rho \gg l_0, \quad (146)$$

As in the case of the phase variance, the plane wave expression (146) is also a reasonable approximation to the more general case of a Gaussian-beam wave for large separation distances and constant κ_0 .

The *phase covariance function* for two points on the phase front in which $\mathbf{r}_2 = -\mathbf{r}_1$ can be approximated by the expression

$$\begin{aligned} B_S(\rho, L) = & 0.64 \sigma_R^2 Q_0^{-5/6} (\kappa_0 \rho)^{5/6} K_{5/6}(\kappa_0 \rho) + 1.18 \sigma_R^2 \left(\frac{k \rho^2}{L} \right)^{5/6} \\ & - 1.33 \sigma_R^2 \Lambda^{5/6} {}_1F_1 \left(-\frac{5}{6}; 1; \frac{\rho^2}{2W^2} \right) - 0.44 \sigma_R^2 \left[a \left(\frac{k \rho^2}{L} \right)^{5/6} \right. \\ & + 0.62 \Lambda^{11/6} \left(\frac{k \rho^2}{L} \right) - 0.97 \sigma_R^2 \operatorname{Re} \left\{ i^{5/6} [1 - (\bar{\Theta} + i \Lambda) d_t]^{5/6} \right. \\ & \times {}_1F_1 \left[-\frac{5}{6}; 1; -\frac{(1 - \bar{\Theta} d_t - i \Lambda d_t) k \rho^2}{4i L d_t} \right] \\ & \left. \left. - (\Lambda d_t)^{5/6} {}_1F_1 \left[-\frac{5}{6}; 1; -\frac{(1 - \bar{\Theta} d_t)^2 k \rho^2}{4L \Lambda d_t^2} \right] \right\} \right], \quad \rho \gg l_0, \quad (147) \end{aligned}$$

Specializations of (147) for the plane wave and spherical wave cases are readily deduced by respectively setting $\Theta = 1$, $\Lambda = 0$ and $\Theta = \Lambda = 0$. Nonetheless, the general expression (147) is dominated by the lead term on the right-hand side.

For a slant path, therefore, we can approximate the covariance function for a Gaussian-beam wave by

$$B_S(\rho, L) = 0.78 k^2 \left(\frac{\rho}{\kappa_0} \right)^{5/6} K_{5/6}(\kappa_0 \rho) \int_0^L C_n^2(z) dz, \quad \rho \gg l_0. \quad (148)$$

We recognize (148) as the geometrical optics approximation to the covariance function for an infinite plane wave.

From Eq. (147) we can infer the *temporal covariance function* (longitudinal component)

$$\begin{aligned} B_S(\tau, 0, L) = & 0.64 \sigma_R^2 Q_0^{-5/6} (\kappa_0 V_\perp \tau)^{5/6} K_{5/6}(\kappa_0 V_\perp \tau) - 0.97 \sigma_R^2 \\ & \times \operatorname{Re} \left\{ i^{5/6} [1 - (\bar{\Theta} + i\Lambda) d_t]^{5/6} {}_1F_1 \left(-\frac{5}{6}; 1; -a_1 \omega_t^2 \tau^2 \right) \right. \\ & \left. - (\Lambda d_t)^{5/6} {}_1F_1 \left(-\frac{5}{6}; 1; -a_2 \omega_t^2 \tau^2 \right) \right\}, \end{aligned} \quad (149)$$

which, in turn, leads to the *phase power spectrum*

$$\begin{aligned} S_S(\omega) = & \frac{4.73 \sigma_R^2 \omega_t^{5/3}}{(\omega^2 + \kappa_0^2 V_\perp^2)^{4/3}} - \frac{0.97 \sigma_R^2}{\omega_t d_t^{5/6}} \operatorname{Re} \left\{ \left(\frac{\omega}{\omega_t} \right)^{-8/3} \left[{}_1F_1 \left(-\frac{5}{6}; -\frac{1}{3}; -\frac{\omega^2}{4a_2 \omega_t^2} \right) \right. \right. \\ & \left. \left. - {}_1F_1 \left(-\frac{5}{6}; -\frac{1}{3}; -\frac{\omega^2}{4a_1 \omega_t^2} \right) \right] + 0.29 i^{4/3} \left[\frac{1}{a_2^{4/3}} {}_1F_1 \left(\frac{1}{2}; \frac{7}{3}; -\frac{\omega^2}{4a_2 \omega_t^2} \right) \right. \right. \\ & \left. \left. - \frac{1}{a_1^{4/3}} {}_1F_1 \left(\frac{1}{2}; \frac{7}{3}; -\frac{\omega^2}{4a_1 \omega_t^2} \right) \right] \right\}. \end{aligned} \quad (150)$$

8.9 Worked Examples

Example 1: A Gaussian beam 6 cm in diameter is focused at a receiver 1000 m from the source. If the wavelength is $1.55 \mu\text{m}$ and atmospheric turbulence along the propagation path is characterized by $C_n^2 = 10^{-14} \text{m}^{-2/3}$, calculate the following quantities based on a Kolmogorov spectrum:

- (a) effective (long-term) beam radius
- (b) on-axis mean irradiance

- (c) longitudinal scintillation index for a tracked beam
- (d) off-axis scintillation index at $r = W$ for a tracked beam
- (e) longitudinal scintillation index for an untracked beam
- (f) off-axis scintillation index at $r = W$ for an untracked beam

Solution: We first calculate the quantities:

$$\Theta_0 = 1 - \frac{L}{F_0} = 0, \quad \Lambda_0 = \frac{2L}{kW_0^2} = 0.5482 \quad \sigma_R^2 = 1.23 C_n^2 k^{7/6} L^{11/6} = 0.20$$

$$\Theta = 0, \quad \Lambda = 1.824, \quad \sqrt{\langle r_c^2 \rangle} = \sqrt{\frac{2.42 C_n^2 L^3}{W_0^{1/3}} {}_2F_1\left(\frac{1}{3}, 1; 4; 1 - |\Theta_0|\right)} = 0.94 \text{ cm}$$

$$(a) \quad W_{LT} = W \sqrt{1 + 1.33 \sigma_R^2 \Lambda^{5/4}} = 1.97 \text{ cm}$$

$$(b) \quad \langle I(0, L) \rangle = \frac{W_0^2}{W_{LT}^2} = 2.32 \text{ W/m}^2$$

$$(c) \quad \sigma_{I,l}^2(L)_{\text{tracked}} = 3.86 \sigma_R^2 \text{Re} \left[i^{5/6} {}_2F_1\left(-\frac{5}{6}, \frac{11}{6}; \frac{17}{6}; \overline{\Theta} + i\Lambda\right) - \frac{11}{16} \Lambda^{5/6} \right] = 0.015$$

$$(d) \quad \sigma_I^2(W, L)_{\text{tracked}} = 4.42 \sigma_R^2 \Lambda^{5/6} \left(\frac{W - \sqrt{\langle r_c^2 \rangle}}{W} \right)^2 + \sigma_{I,l}^2(L)_{\text{tracked}} = 0.28$$

$$(e) \quad \sigma_{I,l}^2(L)_{\text{untracked}} = 4.42 \sigma_R^2 \Lambda^{5/6} \left(\frac{\sigma_{pe}}{W} \right)^2 + \sigma_{I,l}^2(L)_{\text{tracked}} = 0.071$$

$$(f) \quad \sigma_I^2(W, L)_{\text{untracked}} = 4.42 \sigma_R^2 \Lambda^{5/6} \left(\frac{W - \sigma_{pe}}{W} \right)^2 + \sigma_{I,l}^2(L)_{\text{untracked}} = 1.01$$

□

Example 2: Repeat Example 1 for a collimated beam.

Solution: We first calculate the quantities:

$$\Theta_0 = 1 - \frac{L}{F_0} = 1, \quad \Lambda_0 = \frac{2L}{kW_0^2} = 0.5482 \quad \sigma_R^2 = 1.23 C_n^2 k^{7/6} L^{11/6} = 0.20$$

$$\Theta = 0.7689, \quad \Lambda = 0.4215, \quad \sqrt{\langle r_c^2 \rangle} = \sqrt{\frac{2.42 C_n^2 L^3}{W_0^{1/3}} {}_2F_1\left(\frac{1}{3}, 1; 4; 1 - |\Theta_0|\right)} = 0.88 \text{ cm}$$

$$(a) \quad W_{LT} = W \sqrt{1 + 1.33 \sigma_R^2 \Lambda^{5/4}} = 3.64 \text{ cm}$$

$$(b) \quad \langle I(0, L) \rangle = \frac{W_0^2}{W_{LT}^2} = 0.68 \text{ W/m}^2$$

$$(c) \quad \sigma_{I,l}^2(L)_{\text{tracked}} = 3.86 \sigma_R^2 \text{Re} \left[i^{5/6} {}_2F_1 \left(-\frac{5}{6}, \frac{11}{6}; \frac{17}{6}; \bar{\Theta} + i\Lambda \right) - \frac{11}{16} \Lambda^{5/6} \right] \\ = 0.091$$

$$(d) \quad \sigma_I^2(W, L)_{\text{tracked}} = 4.42 \sigma_R^2 \Lambda^{5/6} \left(\frac{W - \sqrt{\langle r_c^2 \rangle}}{W} \right)^2 + \sigma_{I,l}^2(L)_{\text{tracked}} = 0.33$$

$$(e) \quad \sigma_{I,l}^2(L)_{\text{untracked}} = 4.42 \sigma_R^2 \Lambda^{5/6} \left(\frac{\sigma_{pe}}{W} \right)^2 + \sigma_{I,l}^2(L)_{\text{tracked}} = 0.093$$

$$(f) \quad \sigma_I^2(W, L)_{\text{untracked}} = 4.42 \sigma_R^2 \Lambda^{5/6} \left(\frac{W - \sigma_{pe}}{W} \right)^2 + \sigma_{I,l}^2(L)_{\text{untracked}} = 0.46$$

By comparing tracked and untracked beam results in Examples 1 and 2 above, we see that beam wander effects have more impact on convergent beams than on collimated beams, even though the rms beam displacement is almost the same in each case. The reason for this conclusion, of course, is that in the convergent beam case a smaller spot is wandering in the receiver plane, leading to larger off-axis scintillations.

□

Example 3: Given that the log amplitude and phase are defined, respectively, by

$$\chi(\mathbf{r}, L) = \frac{1}{2} [\psi(\mathbf{r}, L) + \psi^*(\mathbf{r}, L)],$$

$$S(\mathbf{r}, L) = \frac{1}{2i} [\psi(\mathbf{r}, L) - \psi^*(\mathbf{r}, L)],$$

show that their mean values can be expressed as

$$\langle \chi(\mathbf{r}, L) \rangle = -\frac{T}{2} - \sigma_\chi^2(0, L)$$

$$\langle S(\mathbf{r}, L) \rangle = -\sigma_{\chi S}^2(0, L),$$

where $\sigma_{\chi S}^2(0, L) = \langle \chi(0, L) S(0, L) \rangle$.

Solution: From definition it follows that

$$\begin{aligned}\langle \chi(\mathbf{r}, L) \rangle &= \frac{1}{2} [\langle \Psi(\mathbf{r}, L) \rangle + \langle \Psi^*(\mathbf{r}, L) \rangle] \\ &= \frac{1}{2} [\langle \Psi_2(\mathbf{r}, L) \rangle + \langle \Psi_2^*(\mathbf{r}, L) \rangle] \\ &= E_1(0, 0) - \frac{1}{4} [E_3(\mathbf{r}, \mathbf{r}) + E_3^*(\mathbf{r}, \mathbf{r})],\end{aligned}$$

which can be expressed as

$$\begin{aligned}\langle \chi(\mathbf{r}, L) \rangle &= -2\pi^2 k^2 L \int_0^1 \int_0^\infty \kappa \Phi_n(\kappa) \left\{ 1 - \exp\left(-\frac{\Lambda L \kappa^2 \xi^2}{k}\right) \right. \\ &\quad \left. \times \cos\left[\frac{L \kappa^2}{k} \xi(1 - \bar{\Theta} \xi)\right] \right\} d\kappa d\xi.\end{aligned}$$

By adding and subtracting the quantity $(1/2)E_2(0,0)$, we can write the above expression as

$$\langle \chi(\mathbf{r}, L) \rangle = -\frac{T}{2} - \sigma_\chi^2(0, L),$$

where T is defined by Eq. (38) in Chap. 6 and the second term is the on-axis log-amplitude variance defined by Eq. (12) with $r = 0$. Of course, for the special case of a plane wave or spherical wave, we have $T = 0$.

Along similar lines we can write

$$\begin{aligned}\langle S(\mathbf{r}, L) \rangle &= \frac{1}{2i} [\langle \Psi(\mathbf{r}, L) \rangle - \langle \Psi^*(\mathbf{r}, L) \rangle] \\ &= \frac{1}{2i} [\langle \Psi_2(\mathbf{r}, L) \rangle - \langle \Psi_2^*(\mathbf{r}, L) \rangle] \\ &= -\frac{1}{4i} [E_3(\mathbf{r}, \mathbf{r}) - E_3^*(\mathbf{r}, \mathbf{r})],\end{aligned}$$

which yields

$$\langle S(\mathbf{r}, L) \rangle = -2\pi^2 k^2 L \int_0^1 \int_0^\infty \kappa \Phi_n(\kappa) \exp\left(-\frac{\Lambda L \kappa^2 \xi^2}{k}\right) \sin\left[\frac{L \kappa^2}{k} \xi(1 - \bar{\Theta} \xi)\right] d\kappa d\xi.$$

By definition, this last expression is recognized [3] as $\sigma_{\chi S}^2(0, L) = \langle \chi(0, L) S(0, L) \rangle$.

□

Example 4: (NUMERICAL) Consider a slant path from the ground to the top of a = building 500 m high and at zenith angle 80 degrees from the observer. Assume $C_n^2(h) = A \exp(-h/100)$, where $A = 1.7 \times 10^{-13} \text{m}^{-2/3}$ and h is altitude from ground level. Given an uplink laser beam with spot radius $W_0 = 1 \text{ cm}$ and

wavelength $\lambda = 1.55 \mu\text{m}$, calculate the on-axis scintillation index (ignoring beam wander effects).

Solution: We first calculate

$$\Theta_0 = 1 - \frac{L}{F_0} = 1, \quad \Lambda_0 = \frac{2L}{kW_0^2} = 14.206$$

$$\Theta = \frac{\Theta_0}{\Theta_0^2 + \Lambda_0^2} = 0.0049, \quad \Lambda = \frac{\Lambda_0}{\Theta_0^2 + \Lambda_0^2} = 0.0700$$

Then, in terms of altitude h , we rewrite Eq. (105) as

$$\sigma_I^2(L) = 8.70 k^{7/6} H^{5/6} \sec^{11/6}(\zeta) \operatorname{Re} \int_0^H C_n^2(h) \{ i^{5/6} (1 - h/H)^{5/6} \\ \times [1 - (\bar{\Theta} + i\Lambda)(1 - h/H)]^{5/6} - \Lambda^{5/6} (1 - h/H)^{5/3} \} dh,$$

where H is the height of the receiver and ζ is zenith angle. The numerical evaluation of this expression yields

$$\sigma_I^2(L) = 0.57.$$

□

Problems

Section 8.2

1. From Eq. (20) for the scintillation index of a Gaussian-beam wave, deduce the plane wave and spherical wave expressions given by Eqs. (21).
2. Under the geometrical optics approximation, the log-amplitude variance for a plane wave is defined by

$$\sigma_x^2(L) = \frac{1}{3} \pi^2 L^3 \int_0^\infty \kappa^5 \Phi_n(\kappa) d\kappa, \quad \sqrt{L/K} \ll l_0.$$

Show that, using the Tatarskii spectrum [Eq. (19) in Chap. 3] and modified spectrum [Eq. (21) in Chap. 3 with $\kappa_0 = 0$], this integral reduces to

$$\sigma_x^2(L) = \begin{cases} 3.19 C_n^2 L^3 l_0^{-7/3}, & \sqrt{L/K} \ll l_0, \quad (\text{Tatarskii spectrum}), \\ 2.41 C_n^2 L^3 l_0^{-7/3}, & \sqrt{L/K} \ll l_0, \quad (\text{Modified spectrum}). \end{cases}$$

3. A collimated beam of diameter 2 cm is propagated along a horizontal path for which the index-of-refraction structure constant is $C_n^2 = 10^{-14} \text{m}^{-2/3}$. If $\lambda = 0.633 \mu\text{m}$, what is the maximum distance the beam can propagate so that the entire diffractive beam ($r \leq W$) remains within the conditions of weak fluctuation theory [i.e., $\sigma_I^2(\mathbf{r}, L) < 1$]? What is the distance if the beam diameter is doubled?
4. A collimated beam of diameter 4 cm is propagated 1 km along a horizontal path for which $C_n^2 = 0.75 \times 10^{-13} \text{m}^{-2/3}$. What is the shortest wavelength that keeps $\sigma_I^2(0, L) < 1$. Assume a Kolmogorov spectrum.
5. By using the Kolmogorov spectrum in (17), derive the scintillation index for the longitudinal component given by (19).
6. The scintillation index of a spherical wave can be deduced from (17) by setting $\Theta = \Lambda = 0$.
 - (a) Following the approach used in deriving the plane wave result (29), perform the integrations on the κ integrals for the spherical wave case and use the small argument approximation in the confluent hypergeometric functions.
 - (b) Define $Q_m = L\kappa_m^2/k$ and assume $Q_m \ll 1$. Use a binomial series on the integrand in ξ in part (a) and obtain a ${}_2F_1$ function after termwise integration.
 - (c) Use identity (H5) in Appendix I and now assume $Q_m \gg 1$ (but not infinite). Combine your results to show that

$$\sigma_{I, \text{sp}}^2(L) \cong 3.86 \sigma_R^2 \left\{ 0.4(1 + 16/Q_m^2)^{5/12} \cos \left[\frac{5}{6} \tan^{-1} \left(\frac{Q_m}{4} \right) \right] - \frac{11}{6} Q_m^{-5/6} \right\}.$$

- (d) Find the limit of part (c) as $Q_m \rightarrow \infty$.

7. Write the longitudinal component of the scintillation index as a sum $\sigma_{I,l}^2(L) = \text{Re}(I_1 - I_2)$, where

$$I_1 = 8\pi^2 k^2 L \int_0^1 \int_0^\infty \kappa \Phi_n(\kappa) e^{-\Lambda L \kappa^2 \xi^2 / k} d\kappa d\xi,$$

$$I_2 = 8\pi^2 k^2 L \int_0^1 \int_0^\infty \kappa \Phi_n(\kappa) \exp\left\{-\frac{iL\kappa^2\xi}{k}[1 - (\bar{\Theta} + i\Lambda)\xi]\right\} d\kappa d\xi.$$

- (a) Under the temporary assumption that $Q_m < 1$, use the von Kármán spectrum to show that

$$\begin{aligned} \sigma_{I,l}^2(L) = 7.075 \sigma_R^2 Q_m^{-5/6} & \left\{ \text{Re} \sum_{n=0}^{\infty} \frac{(-5/6)_n (1)_n}{(2)_n n!} (-iQ_m)^n \right. \\ & \times {}_2F_1(-n, n+1; n+2; \bar{\Theta} + i\Lambda) \\ & \left. - (1 + \Lambda Q_m)^{5/6} {}_2F_1\left(-\frac{5}{6}, 1; \frac{3}{2}; \frac{\Lambda Q_m}{1 + \Lambda Q_m}\right) \right\}. \end{aligned}$$

- (b) Use the approximation

$${}_2F_1(-n, n+1; n+2; x) \approx (1 - 2x/3)^n, \quad n = 0, 1, 2, \dots,$$

and sum the series in (a). Take the real part of your answer and show that it leads to Eq. (30) for $r = 0$.

- (c) From (b), obtain the spherical wave limiting case.

Hint: Your answer should be similar to the answer in Problem 6(c).

- (d) Take the limit of your answer in (b) as $Q_m \rightarrow \infty$ to obtain an approximation valid for the Kolmogorov spectrum.

Section 8.3

8. For a collimated beam propagating 1.2 km through atmospheric turbulence with $W_0 = 1$ cm, $\lambda = 1.06$ μm , $\kappa_0 = 0$, and $C_n^2 = 1.7 \times 10^{-14} \text{ m}^{-2/3}$, what is the scintillation index at $r = W$ for
- a beam that is tracked?
 - a beam that is not tracked?
- Ans.* (a) 0.49 (b) 0.92
9. Repeat Prob. 8 for the case when the beam is focused at the receiver.
10. A 2-cm radius beam is focused at 1500 m and the receiver is located at 800 m. If $\lambda = 1.55$ μm , $\kappa_0 = 0$, and $C_n^2 = 2.5 \times 10^{-14} \text{ m}^{-2/3}$, what is the on-axis scintillation for
- a beam that is tracked?
 - a beam that is not tracked?

Section 8.4

11. Under the geometrical optics approximation $L\kappa^2/k \ll 1$,
 (a) show that the log amplitude covariance function for a plane wave is defined by the integral

$$B_\chi(\rho, L) = \frac{1}{3} \pi^2 L^3 \int_0^\infty \kappa^5 \Phi_n(\kappa) J_0(\kappa \rho) d\kappa, \quad \sqrt{L/k} \ll l_0.$$

- (b) Show that, using the Tatarskii spectrum [Eq. (19) in Chap. 3], the normalized log-amplitude covariance function is

$$b_\chi(\rho, L) = \frac{B_\chi(\rho, L)}{B_\chi(0, L)} = {}_1F_1\left(\frac{7}{6}; 1; -\frac{\kappa_m^2 \rho^2}{4}\right), \quad \sqrt{L/k} \ll l_0.$$

12. Under the geometrical optics approximation $L\kappa^2/k \gg 1$,
 (a) show that the covariance function of log amplitude for a spherical wave is defined by the integral

$$B_\chi(\rho, L) = \pi^2 L^3 \int_0^1 \xi^2 (1 - \xi)^2 \int_0^\infty \kappa^5 \Phi_n(\kappa) J_0(\kappa \xi \rho) d\kappa d\xi, \quad \sqrt{L/k} \ll l_0.$$

- (b) Show that, using the Tatarskii spectrum [Eq. (19) in Chap. 3], the normalized covariance function is

$$b_\chi(\rho, L) = \frac{B_\chi(\rho, L)}{B_\chi(0, L)} = {}_3F_3\left(\frac{7}{6}, \frac{3}{2}, 2; \frac{7}{2}, 3, 1; -\frac{\kappa_m^2 \rho^2}{4}\right),$$

$$\sqrt{L/k} \ll l_0.$$

Section 8.5

13. Given the temporal covariance (56) for an infinite plane wave, show that the corresponding PSD is

$$S_{I, \text{pl}}(\omega) = \frac{6.95 \sigma_R^2}{\omega_t} \text{Re} \left\{ \left(\frac{\omega}{\omega_t} \right)^{-8/3} \left[1 - {}_1F_1\left(-\frac{5}{6}; -\frac{1}{3}; -\frac{i\omega^2}{2\omega_t^2}\right) \right] \right. \\ \left. - 0.72 i^{4/3} {}_1F_1\left(\frac{1}{2}; \frac{7}{3}; -\frac{i\omega^2}{2\omega_t^2}\right) \right\}.$$

14. Given the temporal covariance (58) for a spherical wave, show that the corresponding PSD is

$$S_{I, \text{sp}}(\omega) = \frac{5.47 \sigma_R^2}{\omega_t} \text{Re} \left\{ \left(\frac{\omega}{\omega_t} \right)^{-8/3} \left[1 - {}_1F_1\left(-\frac{5}{6}; -\frac{1}{3}; -\frac{2i\omega^2}{9\omega_t^2}\right) \right] \right. \\ \left. - 0.24 i^{4/3} {}_1F_1\left(\frac{1}{2}; \frac{7}{3}; -\frac{2i\omega^2}{9\omega_t^2}\right) \right\}.$$

15. For frequencies satisfying $\omega \ll \omega_t$, use the results of Probs. 13 and 14 to derive the asymptotic results

$$\omega_t S_I(\omega)/\sigma_I^2(L) \sim \begin{cases} 1.25, & \omega \ll \omega_t \quad (\text{plane wave}) \\ 1.64, & \omega \ll \omega_t \quad (\text{spherical wave}) \end{cases}$$

Section 8.6

16. Establish the equivalence of Eqs. (78) and (79).
 17. Given the validity of Eq. (80), set $\Theta = \Lambda = 0$ to show that

$$\sigma_{S, \text{sp}}^2(L) = 0.64\sigma_R^2 Q_0^{-5/6} (1 - 0.16Q_0^{5/6}).$$

18. Given the integral representation of Eq. (90), show that

$$D_{S, \text{pl}}(\rho, L) = 1.56C_n^2 k^2 L \kappa_0^{-5/3} [1 - (\kappa_0 \rho)^{5/6} K_{5/6}(\kappa_0 \rho)], \quad \rho \gg l_0.$$

19. Show that, for $\kappa_0 \rho \ll 1$, the expression in Prob. 18 reduces to

$$D_{S, \text{pl}}(\rho, L) = 2.91C_n^2 k^2 L \rho^{5/3}, \quad l_0 \ll \rho \ll L_0.$$

20. Use the result of Eq. (94) to obtain an expression for the phase structure function under a geometrical optics approximation that is valid for $\rho \ll l_0$, viz.,

$$D_{S, \text{pl}}(\rho, L) = 1.64 C_n^2 k^2 L l_0^{-1/3} \rho^2, \quad \rho \ll l_0.$$

21. Arising from Eq. (105), deduce the equivalence of the left-hand and right-hand sides of

$$\begin{aligned} & 4\pi^2 k^2 L \int_0^1 \int_0^\infty \kappa \Phi_n(\kappa) \exp\left(-\frac{\Lambda L \kappa^2 \xi^2}{k}\right) J_0[\kappa|(1 - \bar{\Theta}\xi)\mathbf{p} - 2i\Lambda\xi\mathbf{r}|] d\kappa d\xi \\ &= 4\pi^2 k^2 L \int_0^\infty \kappa \Phi_n(\kappa) J_0(\kappa\rho) d\kappa + \frac{1}{2} D_{\text{pl}}(\rho, L) \\ &+ \sigma_r(\mathbf{r}_1, L) + \sigma_r(\mathbf{r}_2, L) - T - \frac{1}{2} \Delta(\mathbf{r}_1, \mathbf{r}_2, L), \end{aligned}$$

22. Set $\Theta = 1$, $\Lambda = 0$ in Eq. (106) and show that in the limiting case of a plane wave it reduces to

$$\begin{aligned} B_{S, \text{pl}}(\rho, L) &= 0.64\sigma_R^2 Q_0^{-5/6} (\kappa_0 \rho)^{5/6} K_{5/6}(\kappa_0 \rho) - 0.97\sigma_R^2 \\ &\times \text{Re} \left[i^{5/6} {}_1F_1\left(-\frac{5}{6}; 1; \frac{ik\rho^2}{2L}\right) - 0.60\left(\frac{k\rho^2}{L}\right)^{5/6} \right], \quad \rho \gg l_0. \end{aligned}$$

23. Set $\Theta = \Lambda = 0$ in Eq. (106) and show that in the limiting case of a spherical wave it reduces to

$$B_{S,sp}(\rho, L) = 0.64\sigma_R^2 Q_0^{-5/6}(\kappa_0 \rho)^{5/6} K_{5/6}(\kappa_0 \rho) + 0.74\sigma_R^2 \left(\frac{k\rho^2}{L}\right)^{5/6} \\ - 0.97\sigma_R^2 \text{Re} \left[0.40i^{5/6} {}_1F_1\left(-\frac{5}{6}; 1; \frac{ik\rho^2}{8L}\right) - 0.075\left(\frac{k\rho^2}{L}\right)^{5/6} \right].$$

24. Starting with Eq. (109), show that it leads to

$$S_{S,pl}(\omega) = \frac{5.82C_n^2 k^2 L V_{\perp}^{5/3}}{(\omega^2 + \kappa_0^2 V_{\perp}^2)^{4/3}}.$$

25. Derive Eq. (109) from Eq. (108).
 26. Given Eq. (113), deduce the limiting case for a plane wave.
 27. Given Eq. (113), deduce the limiting case for a spherical wave.

Section 8.7

28. Solve Example 4 for the case when the transmitter is on top of the building and the receiver is on the ground.
Ans. 0.34
 29. Consider a slant path from the ground to the top of a building 500 m high and at zenith angle 60 degrees from the observer. Assume $C_n^2(h) = A \exp(-h/100)$, where $A = 1.7 \times 10^{-13} \text{ m}^{-2/3}$ and h is altitude from ground level. Given an uplink laser beam with spot radius $W_0 = 1 \text{ cm}$ and wavelength $\lambda = 1.55 \mu\text{m}$,
 (a) calculate the on-axis scintillation index.
 (b) Calculate the scintillation index given a “pointing error” of 0.17 mrad.
 30. Solve Prob. 29 for the case when the transmitter is on top of the building and the receiver is on the ground.
 31. Find a path-averaged value of the refractive-index structure parameter \hat{C}_n^2 that, when used in Eq. (19), will give the same scintillation index as found in Example 4.
-

References

1. R. A. Schmelzter, "Means, variances and covariances for laser beam propagation through a random medium," *Q. Appl. Math.* **24**, 339–354 (1967).
2. D. L. Fried and J. B. Seidman, "Laser beam scintillations in the atmosphere," *J. Opt. Soc. Am.* **57**, 181–185 (1967).
3. A. Ishimaru, *Wave Propagation and Scattering in Random Media* (IEEE Press, Piscataway, New Jersey, 1997); [previously published as Vols I & II by Academic, New York (1978)].
4. W. B. Miller, J. C. Ricklin, and L. C. Andrews, "Log-amplitude variance and wave structure function: a new perspective for Gaussian beams," *J. Opt. Soc. Am. A* **11**, 1653–1660 (1993).
5. W. B. Miller, J. C. Ricklin, and L. C. Andrews, "Effects of the refractive index spectral model on the irradiance variance of a Gaussian beam," *J. Opt. Soc. Am. A* **11**, 2719–2726 (1994).
6. R. J. Hill and S. F. Clifford, "Modified spectrum of atmospheric temperature-fluctuations and its application to optical propagation," *J. Opt. Soc. Am.* **68**, 892–899 (1978).
7. R. J. Sasiela, *Electromagnetic Wave Propagation in Turbulence* (Springer, New York, 1994).
8. L. C. Andrews, R. L. Phillips, and P. T. Yu, "Optical scintillations and fade statistics for a satellite-communication system," *Appl. Opt.* **34**, 7742–7751 (1995); "Optical scintillations and fade statistics for a satellite-communication system: Errata," *Appl. Opt.* **36**, 6068 (1997).
9. J. R. Kerr and J. R. Dunphy, "Experimental effects of finite transmitter apertures on scintillations," *J. Opt. Soc. Am.* **63**, 1–8 (1973).
10. R. Esposito, "Power scintillations due to the wandering of the laser beam," *Proc. IEEE* **55**, 1533–1534 (1967).
11. D. L. Fried, "Statistics of laser beam fade induced by pointing jitter," *Appl. Opt.* **12**, 422–423 (1973).
12. Titterton, "Power reduction and fluctuations caused by narrow laser beam motion in the far field," *Appl. Opt.* **12**, 423–425 (1973).
13. K. Kiasaleh, "On the probability density function of signal intensity in free-space optical communications systems impaired by pointing jitter and turbulence," *Opt. Eng.* **33**, 3748–3757 (1994).
14. O. Steinvall, "Performance of laser tracking of small targets during turbulence and beam jitter," *Opt. Eng.* **43**, 1609–1621 (2004).
15. V. A. Banakh and I. N. Smalikho, "Statistical characteristics of the laser beam propagating along vertical and sloping paths through a turbulent atmosphere," in *Atmospheric Propagation and Remote Sensing II*, A. Kohnle and W. B. Miller, eds., *Proc. SPIE* **1968**, 303–311 (1993).
16. D. L. Fried and H. T. Yura, "Telescope-performance reciprocity for propagation in a turbulent medium," *J. Opt. Soc. Am.* **62**, 600–602 (1972).
17. D. L. Fried and J. D. Cloud, "Propagation of an infinite plane wave in a randomly inhomogeneous medium," *J. Opt. Soc. Am.* **56**, 1667–1676 (1966).

18. D. L. Fried, "Propagation of a spherical wave in a turbulent medium," *J. Opt. Soc. Am.* **57**, 175–180 (1967).
19. A. D. Wheelon, *Electromagnetic Scintillation II. Weak Scattering* (Cambridge University Press, Cambridge, 2003).
20. V. I. Tatarskii, *Wave Propagation in a Turbulent Medium* (McGraw-Hill, New York, 1961), trans. by R. A. Silverman.
21. S. F. Clifford, "Temporal-frequency spectra for a spherical wave propagating through atmospheric turbulence," *J. Opt. Soc. Am.* **61**, 1285–1292 (1971).
22. L. C. Andrews, *Special Functions of Mathematics for Engineers*, 2nd ed. (SPIE Engineering Press, Bellingham, Wash., Oxford University Press, Oxford, 1998).
23. J. D. Shelton, "Turbulence-induced scintillation on Gaussian-beam waves: theoretical predictions and observations from a laser-illuminated satellite," *J. Opt. Soc. Am. A* **12**, 2172–2181 (1995).
24. V. P. Lukin, *Atmospheric Adaptive Optics* (SPIE Optical engineering Press, Bellingham, Wash., 1995); [originally published in Russian (1986)].
25. A. D. Wheelon, *Electromagnetic Scintillation I. Geometrical Optics* (Cambridge University Press, Cambridge, 2001).
26. V. I. Tatarskii, *The Effects of the Turbulent Atmosphere on Wave Propagation* (Keter, Jerusalem, 1971).
27. V. P. Lukin and V. V. Pokasov, "Optical wave phase fluctuations," *Appl. Opt.* **20**, 121–135 (1981).